A review on the Representative Volume Element-based multi-scale simulation of 3D woven high performance thermoset composites manufactured using resin transfer molding process

Anton Trofimov[a], Christophe Ravey[b], Nicolas Droz[c], Daniel Therriault[a], Martin Lévesque[a,]

[a] *Laboratory for Multiscale Mechanics, Polytechnique Montréal, Montréal, QC H3C3A7, Canada*
[b] *Safran Composites, a technology platform of Safran Tech, Itteville, 91760, France*
[c] *Safran Aircraft Engines, Rond point René Ravaud, 77550 Moissy Cramayel, France*

Abstract

This review shows the potential of using the Representative Volume Element concept for the multi-scale simulation of 3D woven high performance thermoset composites manufactured using the Resin Transfer Molding (RTM) process.

Based on the reviewed state of art, this work unleashes the 5 most promising areas for future research that could advance the RTM process optimization.

Area 1: Developing polymer constitutive models databases that rely on the experimental data at all ranges of degrees of cure and temperatures involved in the RTM process. Area 2: Verifying the accuracy of simulation tools on complex parts made of different preform types. Area 3: Increasing computational efficiency of degree of cure- and temperature-dependent viscoelastic constitutive models accounting for the stress relaxation. Area 4: Increasing computational efficiency of the multi-scale homogenization procedure. Area 5: Standardizing experimental measurements during different phases of the RTM process.

Keywords: multi-scale modeling, process optimization, homogenization, 3D woven composite, resin transfer molding

1. Introduction

Resin Transfer Molding (RTM) is a closed mold process used to manufacture geometrically complex high-performance 3D woven fiber reinforced polymer composites for structural applications in aerospace, marine and automotive industries. The RTM process consists in three major steps: (1) injecting a pressurized and heated liquid thermoset polymer into a dry fibrous preform, (2) curing the impregnated system at elevated temperatures until its full consolidation and (3) cooling and

demolding of the consolidated composite part. Figures 1(a), (b) and (c) schematize the injection, the curing and the cooling and demolding phases of the RTM process, respectively.

Predictive tools simulating the RTM process have been developed to help optimizing the manufacturing parameters yielding high quality parts and minimizing expensive trials and errors [2–4]. Figure 2 presents the hierarchy of scales of the 3D woven composite part illustrated in Figure 2(a). Figure 2(b) shows that, at the meso-scale, the composite part is made of tows and of a polymer matrix. Figure 2(c) details that, at the micro-scale, the tows are assumed to be made of bundles of fibers embedded into a polymer matrix. All of these multi-scale features interact with each other and influence the overall part performance. Therefore, an accurate simulation of the RTM process requires a multi-scale procedure [5, 6].

In multi-scale methods, the micro- and meso-scale responses are homogenized and their average response is used for macro-scale simulations. The approach assumes an explicit representation of the micro- and meso-structure using the concept of Representative Volume Element (RVE) [7]. RVEs can be 'artificial' statistically representing microstructures [8–11] or 'real' representations reconstructed from Computed Microtomography (µCT) [12–14] data.

The goals of this review are to show the potential of using the RVE of 3D woven composites concept to simulate the RTM process and to unleash promising areas for future research that together serve the goal of process optimization. The review is organized as follows: Section 2 recalls the concept of the RVE and the homogenization procedure. Section 3 details the types of 3D weave architectures and the generation of their RVEs at the meso-and micro-scales. The works simulating injection, curing, cooling and demolding stages are given in Sections 4, 5 and 6,

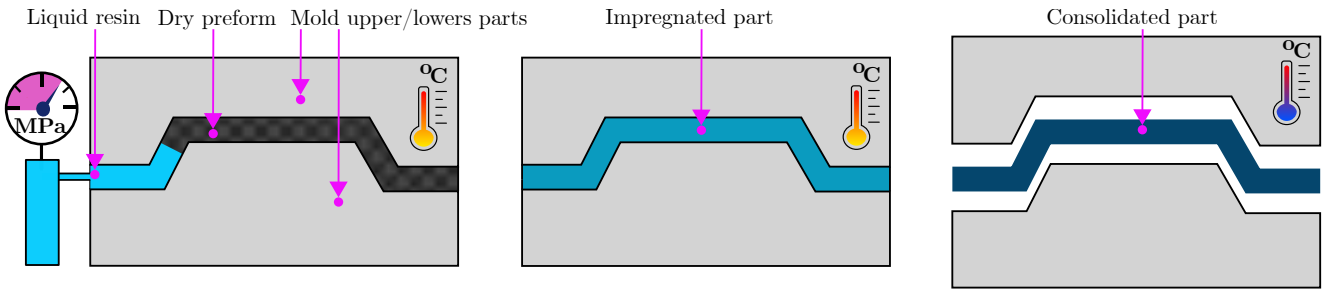

Injection (a) Curing (b) Cooling and demolding (c)

Figure 1: The steps of the RTM process: (a) injecting a pressurized liquid thermoset polymer into a dry fibrous preform, (b) curing the impregnated system at elevated temperatures until its full consolidation and (c) cooling and demolding of the consolidated composite part.

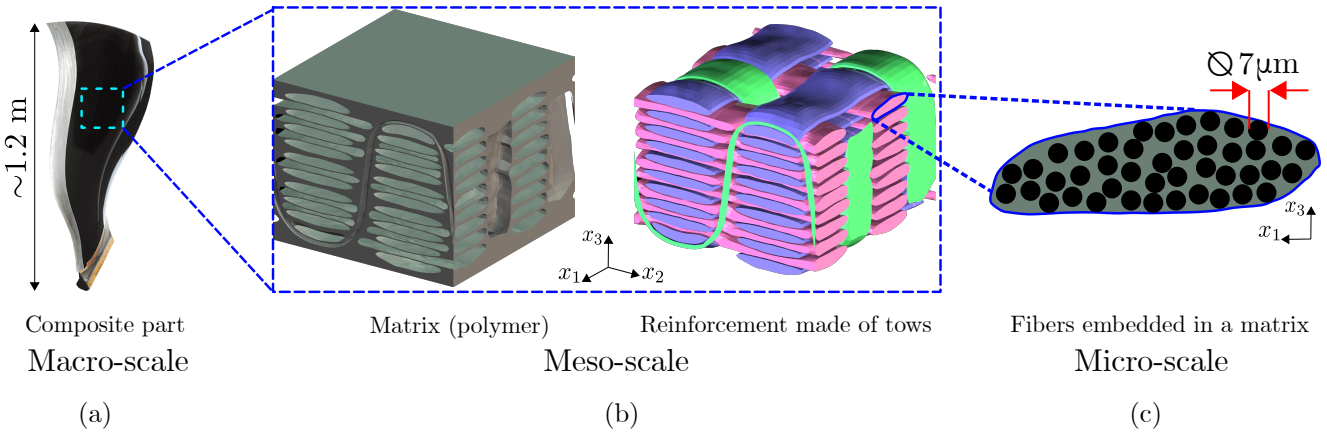

Figure 2: The hierarchical structure of (a) a jet engine 3D woven composite fan blade (GE90-115B) [1](b) at the meso-scale consists of a polymer matrix and reinforcement made of (c) bundles of fibers embedded into a polymer matrix.

respectively. Section 7 summarizes the state of the art in the RTM process optimization. Finally, concluding remarks, challenges, and future opportunities are presented in Section 8.

The modified Voigt notation has been used in our paper. Second-order tensors are defined as six component vectors and symmetric fourth-order tensors are defined as 6×6 matrices. Scalars are expressed as light-faced letters (*i.e.*, a, α and A), second order tensors are represented by boldfaced lowercase Greek letters (*i.e.*, $\boldsymbol{\sigma}$), and fourth-order tensors are represented by boldfaced capital Roman letters (*i.e.*, $\mathbf{C}$).

2. The concept of the RVE and the homogenization procedure

The homogenization procedure relies on the concept of the Representative Volume Element (RVE) introduced by [15] who postulated that the RVE (i) is a volume large enough to be statistically representative of a heterogeneous material; (ii) possesses a constitutive response which is independent of the applied boundary conditions.

RTM manufactured textile composites effective properties are usually obtained through a two-step homogenization strategy using the concept of RVE. First, a homogenization at the micro-scale computes the properties of tows and then a second homogenization procedure results in the overall properties of the composite [5, 6].

2.1. Homogenization of the thermo-chemo-mechanical properties

For linearly thermo-elastic composites, the macroscopic effective thermo-mechanical constitutive behavior is written as [15, 16]:

$$\langle \boldsymbol{\sigma} \rangle = \mathbf{C}^{eff} : \Big(\langle \boldsymbol{\varepsilon} \rangle - \boldsymbol{\alpha}^{eff} \Delta T \Big), \tag{1a}$$

$$\langle \boldsymbol{\varepsilon} \rangle = \mathbf{S}^{eff} : \langle \boldsymbol{\sigma} \rangle + \boldsymbol{\alpha}^{eff} \Delta T, \tag{1b}$$

where $\langle \cdots \rangle$ represents volume averaging, $\mathbf{C}^{eff}$ and $\mathbf{S}^{eff}$ are the effective stiffness and compliance tensors, $\boldsymbol{\alpha}^{eff}$ is the effective coefficient of thermal expansion (CTE), ΔT is a temperature change, $\boldsymbol{\sigma}$ and $\boldsymbol{\varepsilon}$ are the stress and the strain fields inside the RVE, respectively.

The homogenization of the thermo-mechanical properties can be performed analytically using, for example, the Mori-Tanaka scheme detailed in [17], or numerically. The numerical homogenization of mechanical properties ($\mathbf{C}^{eff}$) is usually performed by applying a set of six isothermal ($\Delta T = 0$) strain loadcases (three uniaxial tension and three shear) using periodic boundary conditions (PBC) [18–20]. On the one hand, the numerical homogenization of thermal properties ($\boldsymbol{\alpha}^{eff}$) can be performed by applying a uniform temperature change ΔT while assuming that the surfaces of the RVE are traction free and the nodes on the opposite faces of the RVE coupled using PBC [21]. On the other hand, if the material is assumed to be *linearly thermo-elastic*, computing $\boldsymbol{\alpha}^{eff}$ can be performed from the results of isothermal mechanical simulations only, as shown in [22, 23]. Note that the steps for computing $\boldsymbol{\alpha}^{eff}$ are equivalent to the steps for computing the effective coefficient of chemical shrinkage (CCS, $\boldsymbol{\beta}^{eff}$). Details on using homogenization to compute the thermo-chemo-mechanical properties for 3D woven composites at multiple scales are given in [7, 23].

2.2. Homogenization of the permeability in porous media between the fibers

The macroscopic effective permeability is based on Darcy's law:

$$\langle \mathbf{v} \rangle = -\frac{\boldsymbol{k}^{\text{eff}}}{\mu} \cdot \langle \nabla p \rangle, \tag{2}$$

where $\mathbf{v}$ is the fluid velocity vector, $\boldsymbol{k}^{\text{eff}}$ is the second order permeability tensor containing three principal components, μ is the fluid viscosity, ∇ is the gradient, $\cdot$ is the dot product and p is the pressure coupled with the condition of incompressibility:

$$\nabla \cdot \mathbf{v} = 0. \tag{3}$$

The homogenization of the permeability can be performed analytically as in [24, 25] or numerically [26, 27]. The numerical homogenization of permeability ($\boldsymbol{k}^{\text{eff}}$) can be performed by applying three loadcases (pressure gradients along three global axes) while the opposite faces of the RVE are

coupled using PBCs [28]. Next, the Stokes equation is solved to find the average flow velocity $\langle \mathbf{v} \rangle$ which is then back-substituted into Darcy's law for computing the permeability tensor. Note, in the RTM process where the flow is strongly laminar with typical velocities of 10^{-3} m/s and Reynolds number of about 0.05, the Navier-Stokes equation converges to its linear version, the Stokes equation [29].

2.3. Discussion

For the case of unidirectional composites with high volume fraction of fibers (usual representation of the tow structure at the micro-scale), Khan and Muliana [30], and Zarandi et al. [31] have shown that analytical schemes are accurate tools for estimating $\boldsymbol{\alpha}^{eff}$ and $\boldsymbol{\beta}^{eff}$ while $\boldsymbol{k}^{\text{eff}}$ and mechanical properties need to be homogenized numerically. For the case of complex reinforcement geometries, such as that of 3D woven composites at the meso-scale, analytical homogenization schemes might result in discrepancies as high as $\sim 95\%$, and thus numerical homogenization is required to predict the composite's effective properties [32, 33].

3. Generation of RVEs of weave architectures at the meso-and micro-scales

3D reinforcement architectures are, generally, subdivided into interlock and orthogonal weaves having different types of tows constituted of thousands of aligned fibers [34–36]. Interlock architectures are classified as layer-to-layer and through-the-thickness which include warp (longitudinal) and weft (transverse) tows changing layers at specific points ensuring the connection of the layers. Layer-to-layer architectures feature the interlacing between two successive layers while through-the-thickness architectures include tows that can pass through more than two layers. Figures 3(a) and 3(b) schematize layer-to-layer and through-the-thickness interlock architectures, respectively, with

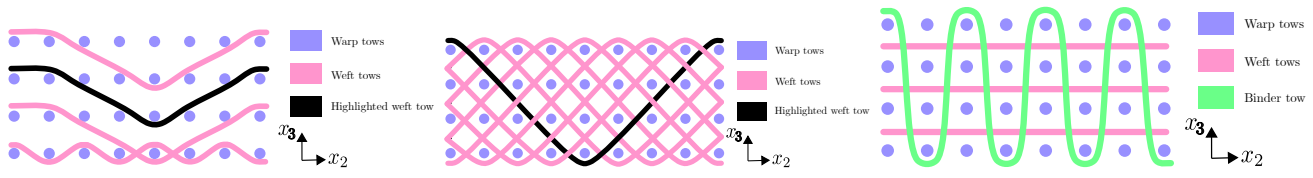

(a) (b) (c)

Figure 3: Schematic representation of 3D reinforcement architectures: (a) layer-to-layer interlock, (b) through-the-thickness interlock and (c) orthogonal. Interlock architectures have two types of tows, warp and weft, while the orthogonal architecture features an additional binder tow.

the highlighted tow visualizing the interlacing path emphasizing the difference between patterns. Figure 3(c) schematizes the orthotropic weave pattern. Orthogonal architectures include warp, weft and binder tows and manufactured such that in-plane tows (warp and weft) are tight together by orthogonal tows (binder) through the thickness.

3.1. RVEs representing 3D woven structures at the meso-scale

3D woven textiles feature a repeated architecture which can be simulated using the RVE. Accurate multi-physics computations using the RVE concept require realistic representations of the tow path and the associated cross sections all along the tow, as well as the intra-tow fiber volume fraction [37, 38]. Over the years, researchers developed many methods to generate RVEs of as-woven geometries which are summarised, for example, by Wielhorski et al. [39], and Gereke and Cherif [40]. Here, we follow the notation of Wielhorski et al. [39] who categorized modeling strategies as the predictive and the descriptive ones.

3.1.1. Predictive modeling of the as-woven geometry

Predictive models simulate weaving pattern evolution from its initial state with straight tows to an as-woven geometry using geometrically-based algorithms or incorporating tows mechanical constitutive models. The tow can be modeled as a homogeneous continuum media or represented as a bundle of virtual fibers [41]. The tows mechanical behavior can be described with hyper-elastic [42, 43] or hypoelastic [44–46] constitutive models allowing for the simulation of large displacements and large shear angles that tows exhibit. Here we give examples of software that use different principles for generating the RVEs architectures using predictive modeling.

TexGen is the open source software developed at the University of Nottingham for generating RVEs based on the local geometrical description of the tows path and cross-sections [47, 48]. Figures 4(a) and 4(b) show examples of meso-scale RVEs generated with the TexGen software simulating layer-to-layer and through-the-thickness weaves, respectively. TexGen allows for the simulation of varied tows cross-sections which can be, for example, measured experimentally. However, geometrical modelling does not take into account the physics of the weaving process and is based on either detailed knowledge of the structure, which is not always available, or assumptions that may result in idealized geometries.

WiseTex is the software developed at KU Leuven that builds RVEs minimizing the bending energy of the tows [49]. A user inputs the weave pattern, tows spacing, tows properties such as

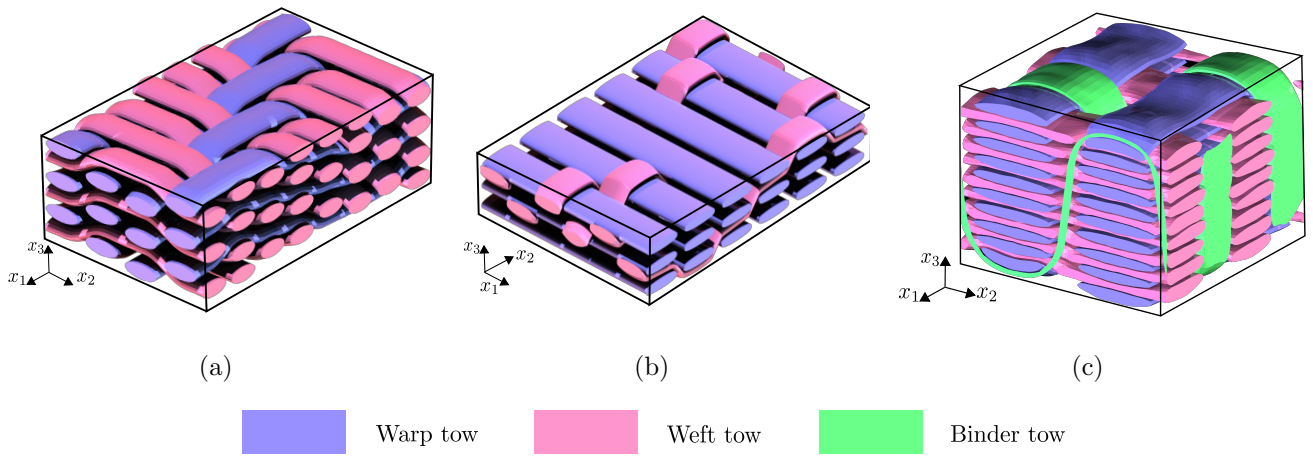

Figure 4: Examples of meso-scale RVEs generated with predictive models: (a) layer-to-layer interlock; (b) through-the-thickness interlock and (c) orthogonal weaves. Figures (a) and (b) were generated using TexGen while (c) was developed using Digital Fabric Mechanics Analyzer (DFMA).

cross-section geometry, bending rigidity, transverse compressive stiffness and the software computes polynomial coefficients describing the tows path and the ratio of the major to minor axes of the tows cross-section. The approach is based on mechanical principles. However, the major difficulties lie in defining tows bending rigidity and transverse stiffness. Moreover, an assumption of the idealized tows cross-section may generate RVEs with the fibers volume fractions that are not in line with those experimentally measured [50].

Digital Fabric Mechanics Analyzer (DFMA) is the software developed at the Kansas State University that builds RVEs minimizing the energy required to deform bundles of fibers constituting tows into the final weave architecture [51, 52]. Figure 4(c) presents an example of meso-scale RVEs generated with the DFMA software simulating the orthogonal weave. Initially, straight homogeneous tows representing a weave pattern are assumed to be in tension. The structure is then sequentially discretized into a bundles of fibers and relaxed until all nodal forces are in equilibrium and all nodal velocities approach zero. The approach simulates the weaving procedure and results in realistic RVE architectures. However, the difficulty lies in removing tows interpenetrations which, usually, requires considerable post-processing efforts [53].

3.1.2. Descriptive modeling of as-woven geometry

Descriptive models construct RVEs by converting a set of µCT images into a numerical representation. The process of converting includes the segmentation of the composite constituents

(different types of tows and polymer matrix) and computation of the tows local orientations.

The segmentation could be performed by discretizing a scanned specimen into voxels (cubic sub-volumes) that are featured with an orientation vector, the degree of anisotropy ranging from 0 for isotropic components to 1 for anisotropic components and the averaged grey value describing the constituent computed with the structure tensor [54–56]. The voxels are then thersholded [55], clustered using k-means [55] or classified using the Gaussian Mixture Model (GMM) [56].

Figure 5 shows the results of segmentation using thresholding and k-means clustering of a 3D woven orthogonal composite µCT image reported by Straumit et al. [55]. Figure 5(a) presents the µCT image of a composite containing the warp, the weft and the binder tows, the matrix and the air. Figures 5(b) and 5(c) detail the results of a segmentation by thresholding the degree of anisotropy and by k-means clustering by the degree of anisotropy and warp component of the orientation vector, respectively. Straumit et al. concluded [55] that thresholding was rather impractical as it was not capable of distinguishing between the types of tows because of the ring artifacts (local distortion in the vector field near the center of the ring structures) originated from the μCT. The authors reported that the k-means clustering performed better allowing for separating the different

(a) (b) (c)

Figure 5: The results of segmentation using thresholidng and k-means clustering published by Straumit et al. [55]: (a) a µCT image, (b) the segmentation by thresholding the degree of anisotropy and (c) the segmentation by k-means clustering by the degree of anisotropy and warp component of the orientation vector. Reprinted from Composites Part A: Applied Science and Manufacturing, 69, I. Straumit, S. V. Lomov, M. Wevers, Quantification of the internal structure and automatic generation of voxel models of textile composites from X-ray computed tomography data, 150-158, Copyright (2015), with permission from Elsevier.

types of tows and the matrix while failed to recognize the air as a separate component.

Figure 6 shows the results of segmentation using a GMM model of a 3D woven orthogonal composite specimen reported by Liu et al. [56]. Figure 6(a) presents the µCT-based 3D model of a composite containing the warp, the weft and the binder tows (the matrix was hidden). Figure 6(b) details the results of a segmentation by a GMM model. Liu et al. concluded [56] that their procedure successfully identified the matrix, the weft and the warp tows, while failed to predict the binder's path and its thickness variation along the path. The authors reported that increasing the accuracy may require additional manual post-processing.

The segmentation could also be performed using machine learning and neural networks. Ali et al. [58] developed a procedure based on the deep convolutional neural network to generate a 3D woven structure with orthogonal weave from µCT images and compared predicted volume fractions of warp, weft and binder tows, and pores against those measured in a real structure. Ali et al. reported differences smaller than 5% for all features, except the binder tows for which an error was found to be $\sim 30\%$. However, neural networks require training data sets which involves significant manual work associated to the post processing of µCT images. To overcome this problem, Mendoza et al. [57] proposed training neural networks on artificial data sets created using Finite Element

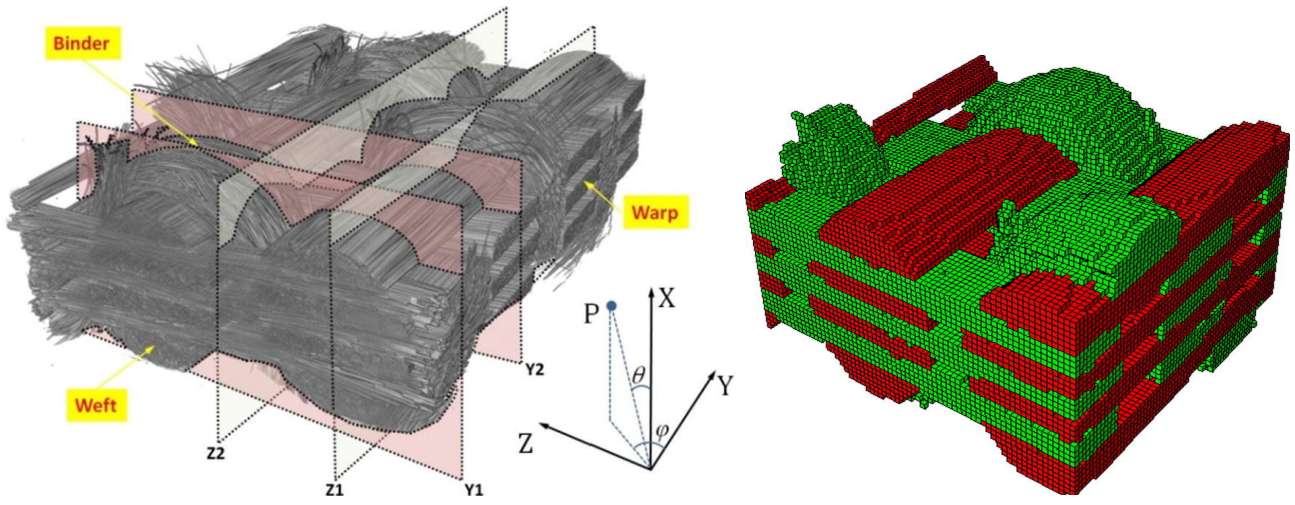

(a) (b)

Figure 6: The results of the segmentation using a GMM model reported by Liu et al. [56]: (a) a µCT 3D model of a composite sample, (b) a reconstructed model. Reprinted from Composite Structures, 179, Y. Liu, I. Straumit, D. Vasiukov, S. V. Lomov, S. Panier, Prediction of linear and non-linear behavior of 3D woven composite using mesoscopic voxel models reconstructed from X-ray micro-tomography, 568-579, Copyright (2017), with permission from Elsevier.

(FE) simulations that allow for generating large annotated data without manual work. Figure 7(a) shows the µCT-based 3D model of a composite containing the warp and the weft tows while Figure 7(b) depicts the reconstructed numerical model. Mendoza et al. compared tow paths (using the Haussdorf metric) and intra-tow volume fractions predicted numerically against those measured experimentally of the 3D woven composite featuring the layer-to-layer weave. Authors concluded that the vast majority of tows have rather small Haussdorf distances (< 0.5) with very few outliers while predicted intra-tow volume fractions were less accurate as they ranged from 55% to 90% when in reality it is difficult to exceed 70–75%. Simultaneously with solving the segmentation problem, the procedure of Mendoza et al. [57] described each tow using the respective key points which allowed for constructing a conformal FE meshing presented in Figure 7(c).

3.2. RVEs representing tows at the micro-scale

In reality, the bundles of fibers constituting tows are distributed irregularly [59, 60]. However, it is common to idealize the structure as straight cylinders with ellipsoidal cross-sections having hexagonal, square or random packings. For illustration purposes, Figures 8(a), 8(b), 8(c) schematize bundles of fibers inside the tows and their corresponding RVEs for a hexagonal packing having a volume fraction of fibers of 40%, a square packing having a volume fraction of fibers of 40% and a random packing having a volume fraction of fibers of 25%, respectively.

The choice of an idealized packing depends on the fibers volume fraction which is, usually, in the range of $\sim 60\%$ to $\sim 75\%$ for 3D woven composites [61]. For a periodic RVE containing cylinders with circular cross-section, the hexagonal packing allows for the highest densities, up to

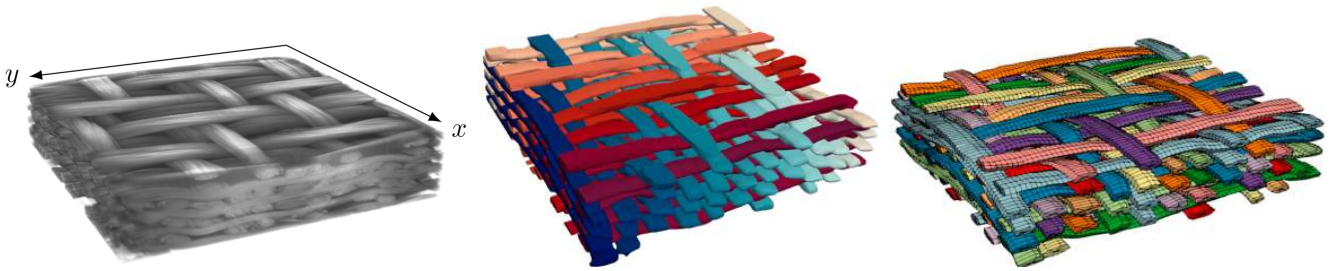

(a) (b) (c)

Figure 7: The results of the segmentation using neural networks reported by Mendoza et al. [57]: (a) a µCT 3D model of a composite specimen, (b) a reconstructed model and (c) the resulting FE surface mesh of the reinforcement. Reprinted from Composites Science and Technology, 213, A. Mendoza, R. Trullo, Y. Wielhorski, Descriptive modeling of textiles using FE simulations and deep learning, 108897, Copyright (2021), with permission from Elsevier.

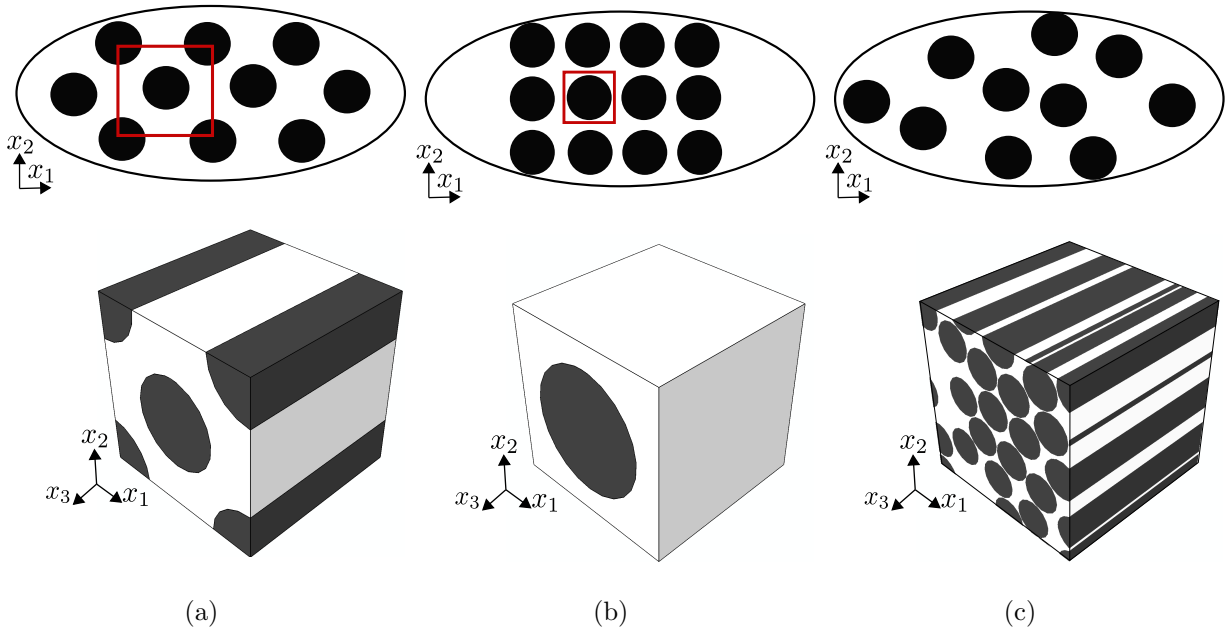

Figure 8: Schematic representations of bundles of fibers inside the tows and their corresponding RVEs for (a) a hexagonal packing having a 40% of fibers volume fraction, (b) a square packing having a fiber volume fraction of 40% and (c) a random packing having a fiber volume fraction of 25%.

$\sim 90.6\%$, while the square packing is limited to $\sim 78.5\%$ and the random packing to $\sim 65\%$ [62]. The effects of fiber packing arrangements (hexagonal, square and random) on the overall elastic properties, CTE and von Mises stress predictions for fiber volume fractions ranging from 10% to 60% are discussed in [59, 63]. For the effective elastic properties, Huang et al. [59] showed that hexagonal and random packings are in a good agreement for the whole range of considered volume fractions while the square packing results in discrepancies that are growing progressively with the volume fractions, up to $\sim 20\%$, and results in a transverse anisotropy. In the case of CTE, the predictions from all arrangements were found to be in an excellent agreement [59].

Building RVEs for the hexagonal and square packing is straightforward, while generating RVEs for random distributions requires packing algorithms that are well established in the literature and include, for example, Molecular Dynamics (MD) based algorithms [64–66], the random sequential adsorption (RSA) algorithm [67], Monte-Carlo simulation based algorithms [18], collective rearrangement methods (CRM) [8, 11] and random sequential expansion (RSE) algorithms [68]. Park et al. [62] presented a new approach for simultaneously generating RVEs with fiber volume fractions ranging from 5% to 65%. The authors proposed generating RVEs by randomly removing fibers from a so-called master RVE having the highest fibers content to reach the target volume fraction.

Park et al. generated a master RVE consisting of 100 fibers and 65% of fiber volume fraction using the RSE algorithm and were randomly eliminating fibers to match the predefined volume fractions ranging from 60% to 5%. The developed approach by [62] allows creating only one FEM model of the master RVE from which other FEM models can be constructed simply reassigning properties of fibers to those of the matrix. This procedure could speed up the RTM process simulations when tows consisting as-woven geometry are modelled with non-uniform cross-sections resulting in non-uniform local fiber volume fractions. The FE computations of RVEs representing tows with a non-uniform local fiber volume fraction would therefore require constructing only one master RVE which could be beneficial especially for large number of FEs.

3.3. Discussion

Accurate numerical representation of textiles' multi-scale geometries requires significant manual work, otherwise geometries are idealized. With a maturity of image post-processing using machine learning and neural networks, generating RVEs based on experimental observations could be a promising way to accurately represent as-woven geometries on multiple scales.

Constructing RVEs for subsequent process simulations requires accurate representations of the tow's path, it's cross-section, local fibers volume fraction and a robust meshing strategy. The complexity of the meshing step is defined by the approaches used at earlier stages. Currently, the majority of progress deals with the individual steps while only a few works provided a complete procedure creating ready-to-run RVEs [69]. Integrating solutions of each step into a single chain, where every step could be tuned, would allow computing uncertainties and errors that can be further optimized.

4. Simulation of the injecting phase of the RTM process

Figure 9(a) schematizes the liquid resin injection into the fibrous preform during the in-mold phase of the RTM process at the macro-scale. The resin injection and the voids formation at the macro-scale are usually modeled with numerical tools like PAM-RTM, Liquid Injection Molding Simulation (LIMS), RTM-Worx or an open source OpenFoam [2, 70–73] that are based on Darcy's law. When Darcy's law (Equation (2)), is coupled with the condition of incompressibility (Equation (3)) the complex interactions between the polymer and the preform are characterized by the $\boldsymbol{k}^{\text{macro}}$ whose accuracy defines the validity of the injection simulations. In 3D interlocks, accurate

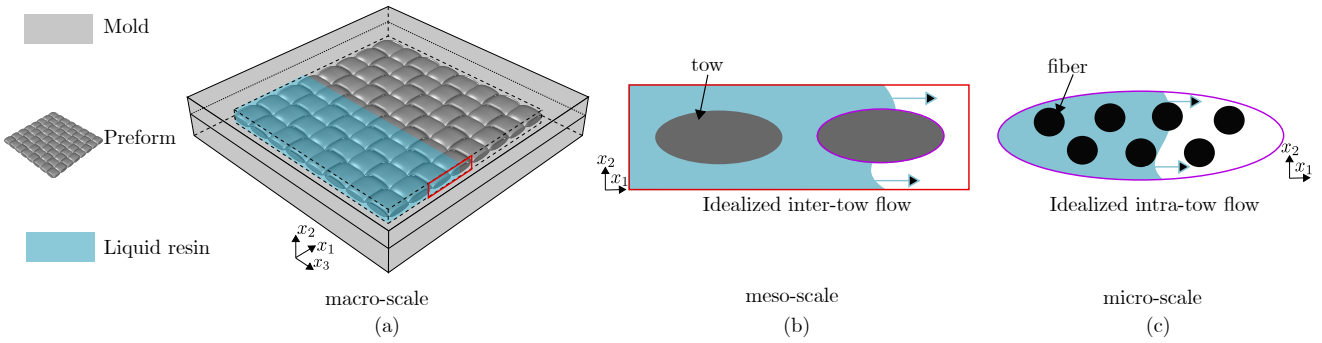

Figure 9: Schematic representation of a liquid resin injection into a fibrous preform during the in-mold phase of the RTM process. The flow is classified as: (a) macroscopic at the part's level; (b) inter-tow at the meso-scale and (c) intra-tow at the micro-scale.

determination of full permeability tensor $\boldsymbol{k}^{\text{macro}}$ (with its skew terms) is especially important since the flow principal directions are often not obvious to determine.

A dry preform is considered as a dual scale medium and, thus, the flow is classified as inter-tow between the tows sketched in Figure 9(b) and intra-tow inside the bundles of fibers schematized in Figure 9(c) [74, 75]. Prediction of the $\boldsymbol{k}^{\text{macro}}$ accounting for a dual scale medium is mathematically justified in [28, 76–78] and includes computation of the tows permeability at the micro-scale which is then input into the final simulations at the meso-scale.

4.1. Permeability predictions at micro-scale

At the micro-scale, Karaki et al. [27] performed a detailed comparison of analytical and numerical predictions of tows longitudinal (k_L^{tow}) and transversal (k_T^{tow}) components of the permeability tensor against available experimental data. The authors considered seven analytical models predicting k_L^{tow} and seventeen model estimating k_T^{tow}. Karaki et al. [27] considered systems having fibers volume fraction ranging from 10% to 77%, and from 11% to 55% for the k_L^{tow} and k_T^{tow}, respectively. The range of considered volume fraction was constrained by the availability of the literature data. Karaki et al. [27] showed that the analytical models of Tamayol and Bahrami [79], and Cai and Berdichevsky [80] using a square fiber packing resulted in discrepancies smaller than $\sim 6\%$ for the whole range of volume fractions. Also, Karaki et al. [27] showed that the analytical models of Cai and Berdichevsky [80], Gebart [81], Drummond and Tahir [82], and Kuwabara [83] using hexagonal fiber packing resulted in discrepancies smaller than $\sim 10\%$ for the whole range of volume fractions.

Zarandi et al. [31] compared tow permeability components computed numerically against those predicted by eighteen analytical models and measured experimentally. Zarandi et al. considered

systems having fibers volume fraction of 50%, 55% and 60%. For the k_L^{tow}, Westhuizen and Du Plessi model [84] resulted in the lowest discrepancy of $\sim 40\%$ as compared to the measured value, while the best numerical prediction resulted in $\sim 30\%$ of discrepancy. For the k_T^{tow}, Bruschke-Advani [85] resulted in the lowest discrepancy of $\sim 10\%$ as compared to the measured value, while the best numerical prediction resulted in $\sim 7\%$ of discrepancy. Note that Zarandi et al. reported a discrepancy of $\sim 20\%$ between two measured transverse components which limits the accuracy of considered analytical models as they assume their equivalence.

From the comprehensive overviews of Karaki et al. [27] and Zarandi et al. [31], it can be concluded that there is no single analytical model that can predict both k_L^{tow} and k_T^{tow} at all levels of fibers volume fractions.

4.2. Permeability predictions at meso-scale

At the meso-scale, Bodaghi [86] presented a comprehensive review on the variability of a preform permeability highlighting the importance of a realistic representation of the as-woven geometries including such parameters as compaction, fiber volume fraction, fiber rearrangements, tow shape and spacing etc. The availability of numerical tools generating textiles RVEs enabled a significant number of works predicting permeability tensors of various types of weaving architectures [87–89]. Swery et al. [90] compared numerical estimations of permeability using WiseTex generated RVEs of various textiles against the second permeability benchmark exercise [91]. The authors computed up to $\sim$5 times higher values of permeability tensor components than those measured experimentally and, as a result, suggested that improving the simulation validity requires more accurate local representations of a textile architectures accounting for nesting and tows deformations. Swery et al. [92] numerically studied the effects of the number of layers, ply shift and applied compaction on permeability, isolating the influence of individual parameters. The authors concluded that the tow gap width had the most important influence on the permeability followed by the local textile deformations.

Ali et al. [93] generated as-woven geometries of orthogonal and angle interlock composites from X-ray micro-computed tomography (XCT) images to predict out-of-plane permeability tensors components for different compaction levels of the same textile having volume fractions of 47%, 58%, 61% and 67%. The authors compared their predictions against experimental data of Alhussein et al. [94] and reported an average discrepancy of 25%. The authors showed that orthogonal preforms experience greater resistance to compaction, when compared to angle interlock preforms, which

resulted in higher out-of-plane permeability tensors components.

Ali et al. [95] extended their previous study [93] and computed in-plane permeability tensor components using commercial software GeoDict. Ali et al. measured in-plane permeability tensor components using the constant injection pressure radial flow method and compared their values against those predicted numerically. The most significant discrepancies 372% and 98%, were found in the case of the lowest considered compaction level of 47% for longitudinal and transverse components, respectively. The most accurate predictions were reported for the compaction level of 61% resulting in a discrepancy smaller than $\sim 2\%$ for both longitudinal and transverse components. For the rest of compactions (58% and 67%), the relative errors were no more than $\sim 30\%$ for both components. Using fluid flow visualization, Ali et al. showed that the polymer traveled through the inter-tow channels, the size of which depend on the compaction level, until blocked by the binder tow. The authors concluded that the local geometrical parameters of an as-woven geometry, such as the sizes of the inter-tow channels and the shape of the binder tow, played a vital role in determining the overall in-plane permeability values highlighting the importance of realistic textile representation.

Ali et al. [96] reconstructed orthogonal as-woven geometry from XCT images and predicted all components of permeability tensor of a 3D angle interlock composite at different compaction levels, namely 50.6%, 53.34% and 56.4% using commercial software GeoDict and compared their predictions against measured values of Alhussein et al. [94]. In the case of transverse and longitudinal components, the most significant discrepancies of up to one order of magnitude were found in the case of the smallest compaction level of 50.6% for both, while computed values for the rest of compaction levels were quantitative having $\sim 10\%$ of accuracy. Ali et al. [96] suggested that the error was due to the difference in the specimen size which was smaller than that of Alhussein et al. [94]. Another source of errors could be the fact that Ali et al. [96] neglected the intra-tow flow in their simulation which could be more relevant for higher compaction levels. In the case of out-of-plane components, simulations were able to quantitatively predict measured values with a relative error of less than 10%.

4.3. Discussion

The validity of permeability predictions highly depends on the realistic as-woven geometry representation using RVEs at multiple scales and standardized numerical approach. The level of fidelity in RVEs needs to be identified by performing experimentally validated parametric studies

computing key micro- and meso-structural parameters that influence the accuracy of the simulations the most. Only limited works showed sensitivity analyses to evaluate the influence of the local RVE geometry on the prediction of the overall permeability [92, 97]. Recent international benchmarks on the image-based permeability predictions showed that computed by different research groups values could significantly scatter. For the case of micro-scale predictions, the scatter of up to two orders of magnitude was reported in [98, 99], which was reduced to 14% and 25% for longitudinal and transverse permeability respectively after the elimination of inconsistent results. Therefore, international benchmarks indicate a need for standardization of numerical predictions.

At the same time, international benchmark exercises on in-plane [91, 100, 101] and out-of- plane [102] permeability components measurements show that the obtained values by different research groups significantly scatter (up to 44% for the in-plane and up to several order of magnitudes for the out-of-plane) and, therefore, reliable measurements require further standardization.

Therefore, combined progress in realistic representation of as-woven structure at multiple scales and standardized numerical and measuring procedures would allow for a more rigorous comparison between numerical predictions and experimental data.

5. Simulation of the curing phase of the RTM process

Figure 10 shows a schematic representation of the curing phase of the RTM process. Figure 10(a) details a fully impregnated macroscopic part being subjected to pressure and temperature cycles. Figure 10(b) presents a typical pressure, temperature and degree of cure evolution (computed with the Kamal-Sourour model discussed in [7]) during the curing phase of the RTM process. Based on the pressure evolution, the process can be divided into two stages: the application of a consolidation pressure p^{con} to maintain the pressure level ((3) in Figure 10(b)) and the reduction of the part/mold adhesion leading to a pressure decrease towards atmospheric pressure p^{atm} ((4) in Figure 10(b)). Based on the temperature evolution, the process can be divided into two stages: curing with a temperature ramp starting at injection temperature T^{inj} ((2) in Figure 10(b)) followed by a dwell at T^{dwell} ((2) in Figure 10(b)). In Figure 10(b)(b), t^{inj} is the injection time, t^{cure} is the time from the start of an injection until the end of curing and t^{cool} is the time from the start of an injection until the end of cooling and demolding phase.

A complex time and temperature dependent process during the curing phase generates residual stresses build-up that might eventually lead to geometrical distortions of a part when demolded.

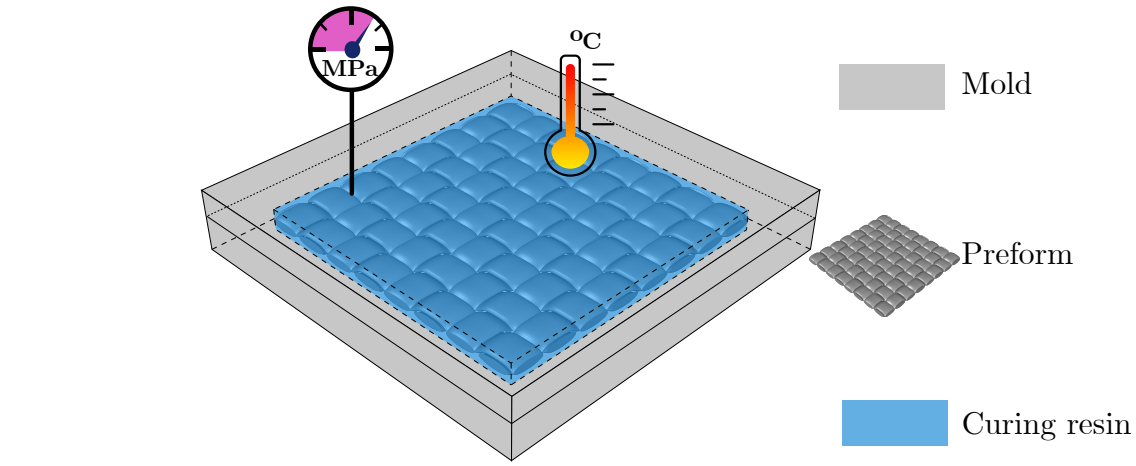

(a)

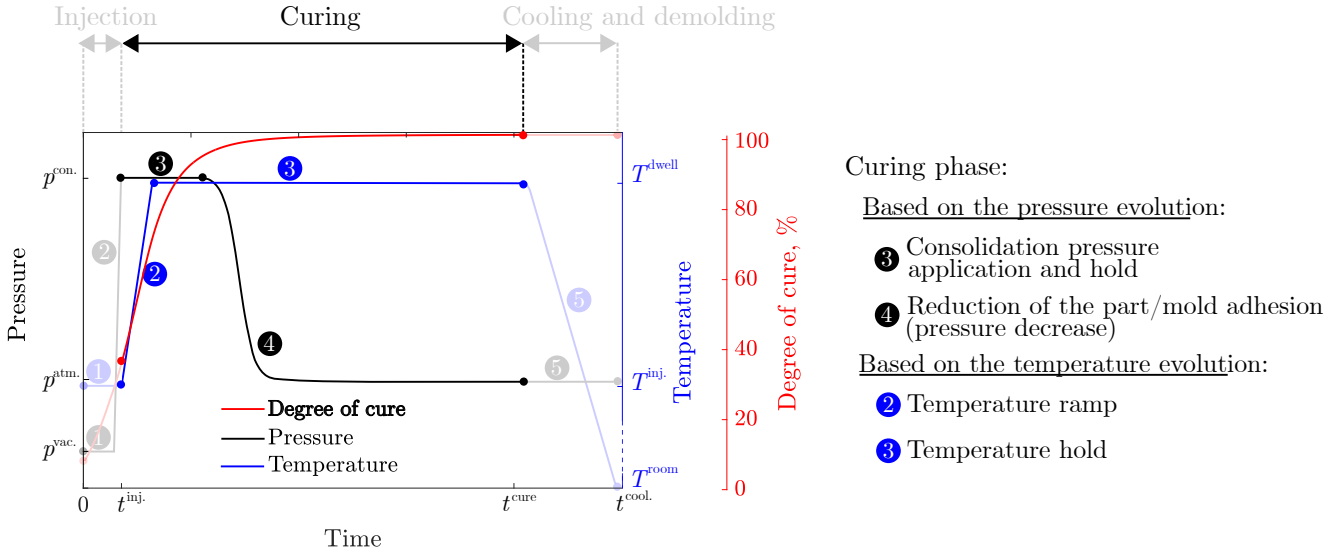

(b)

Figure 10: Schematic representation of the curing phase of the RTM process: (a) a fully impregnated macroscopic part is subjected to pressure and temperature cycles; (b) a common pressure, temperature and degree of cure evolution during the curing phase of the RTM process. Based on the pressure evolution, the process can be divided into two stages: the application of a consolidation pressure p^{con} to maintain the pressure level and the reduction of the part/mold adhesion leading to a pressure decrease towards atmosphere pressure p^{atm}. Based on the temperature evolution, the process can be divided into two stages: curing with a temperature ramp starting at injection temperature T^{inj} followed by a dwell at T^{dwell}. In Figure (b), t^{inj} is the injection time, t^{cure} is the time from the start of an injection until the end of curing and t^{cool} is the time from the start of an injection until the end of cooling and demolding phase. The evolution of the degree of cure was computed with the Kamal-Sourour model as discussed in [7].

The residual stresses mainly result from the dissimilar fibers and polymer coefficients of thermal expansion, the polymer cure shrinkage and the polymer evolution from a viscous liquid to a viscoelastic solid when crossing the gelation point (α_{gel}) [103–109]. The application of a consolidation pressure during curing potentially limits pore growth and collapses existing voids that reduce the part's quality [110–112]. For the case of a pure polymer, Pupin et al. [112] proposed applying a consolidation pressure when the polymer's loss and storage moduli are equal, which is usually corresponding to a degree of cure ranging from 85% to 93% to avoid the creation of harmful porosities. However, for the case of composites, the presence of a reinforcement generates a heterogeneous pressure transmission within the part and may reduce the effect of a consolidation pressure, thus increasing porosity inside the composite [113].

Loos et al. [114] and Svanberg et al. [115] developed a sequentially modular approach to simulate the thermo-chemo-mechanical phenomena involved during the RTM process. The approach starts by computing temperature and degree of cure evolution within the part during the RTM process using coupled thermo-chemical models [104, 116]. The resulting time dependent temperature and degree of cure distributions are input as solution-independent conditions into a constitutive model computing the total strain response $\boldsymbol{\varepsilon}^{\text{tot}}$ of a 3D woven composite as [4, 117]:

$$\boldsymbol{\varepsilon}^{\text{tot}} = \boldsymbol{\varepsilon}^{\text{mech}} + \boldsymbol{\varepsilon}^{\text{non-mech}}, \tag{4}$$

where $\boldsymbol{\varepsilon}^{\text{mech}}$ are mechanical strains and $\boldsymbol{\varepsilon}^{\text{non-mech}} = \boldsymbol{\varepsilon}^{\text{non-mech}}_{\text{CCS}} + \boldsymbol{\varepsilon}^{\text{non-mech}}_{\text{CTE}}$, where $\boldsymbol{\varepsilon}^{\text{non-mech}}_{\text{CCS}}$ and $\boldsymbol{\varepsilon}^{\text{non-mech}}_{\text{CTE}}$ are the stress free strains associated to the chemical shrinkage and thermal expansion, respectively.

Computing $\boldsymbol{\varepsilon}^{\text{tot}}$ at the macro-scale requires a robust time, temperature and degree of cure dependent thermo-chemo-mechanical constitutive model of a polymer and an efficient two step homogenization procedure, as detailed in Section 2.

Researchers reported that, before α_{gel}, the resin is compliant enough to immediately relax residual stresses [118–120]. Consequently, thermo-chemo-mechanical constitutive models are applicable for degrees of cure higher than that of α_{gel}.

Fibers constituting tows are usually assumed as linearly elastic while the polymer matrix has been assumed to obey various constitutive models that accounted for the different thermo-chemo-mechanical phenomena active during the RTM process that are discussed, for example, in Zobeiry et al. [121].

The Cure Hardening Instantaneously Linear Elastic (CHILE) [122] model accounts for a

temperature and degree of cure dependency of the elastic modulus. Wang et.al [123] used a multi-scale approach to compute the residual strains inside a L-shaped layer-to-layer interlock composite part during curing starting at a degree of cure of 25% and compared predicted strains against those measured with Fiber Bragg Grating sensors. Wang et.al [123] simulated mechanical behavior of a resin using the CHILE model with a constant Poisson's ratio while the non-mechanical behavior was assumed to be linearly dependent on the temperature and degree of cure. At the micro-scale, fibers were assumed to have hexagonal packing in the polymer matrix and the thermo-mechanical properties of tows were homogenized numerically, as discussed in Section 2.1. At the meso-scale, authors used custom geometrical modeling of the RVE assuming a straight path for the tows and constant octagonal-shaped tow's cross-sections. The curing phase was simulated by applying a temperature cure cycle. The authors reported qualitative predictions of the strain evolution in the longitudinal direction for the whole curing stage and quantitative predictions for the degrees of cure larger than ~ 80 % with an average relative error of $\sim 10\%$. Increasing accuracy might require more realistic representations of the as-woven geometry and a more complex constitutive thermo-chemo-mechanical model of a pure resin.

Detailed benchmarkings of different elastic and viscoelastic constitutive models simulating residual stresses were reported in [4, 117, 121, 124]. It was shown that, since the CHILE model neglects creep and relaxation effects, it might be reliable in predicting only the final process-induced warpage and residual stress/strain state, for materials and cure cycles where the elastic modulus monotonously increases (i.e., no devitrification or softening response). Consequently, the accurate prediction of internal stresses evolution during the RTM process requires complex viscoelastic constitutive models.

Linearly viscoelastic constitutive models based on the framework of the thermodynamics of irreversible processes [125–127] were widely used in multi-scale simulation predicting creep and relaxation behavior of various composites [128–132]. However, the curing phase is associated with the degree of cure evolution and, therefore, needs to be included. Courtois et al. [133] developed a degree of cure- and temperature-dependent viscoelastic constitutive model for epoxy resins below their glass transition temperature (T_g). This model was extended to simulate creep strains below the resin's T_g in a 3D interlock composite [134]. Trofimov et al. [7] extended the work of Courtois et al. [134] and developed a multi-scale anisotropic thermo-chemo-viscoelastic simulation procedure below and above T_g for predicting stresses and strains in a non-flat layer-to-layer composite during

the curing and post-curing phases of the RTM process. For a pure resin, Trofimov et al. [7] assumed a degree of cure- and temperature-dependent viscoelastic constitutive mechanical model with a constant Poisson's ratio while the non-mechanical behavior was assumed to vary linearly with respect to the temperature and degree of cure. At the micro-scale, fibers were assumed to have a hexagonal packing in the polymer matrix and the thermo-mechanical properties of the tows were homogenized numerically, as discussed in Section 2.1. At the meso-scale, Trofimov et al. used WiseTex to generate the RVE and the curing phase was simulated by applying a curing temperature profile similar to that of Figure 10. In the work of Trofimov et al. [7], the simulation procedure was validated experimentally against the measured distortion of the demolded part (discussed in Section 7). Strains at the curing phase were not measured, however.

Trofimov et al. [135] developed a computationally efficient multi-scale thermo-chemo-mechanical procedure combining up-scale and resolved-scale simulations to predict the pressure evolution inside a 3D woven composite part during the curing phase of the RTM process. The developed procedure benefited from the linearity of a previously developed [134] anisotropic temperature- and degree of cure-dependent thermo-chemo-viscoelastic constitutive law which allowed for relatively fast predictions at different length-scales. The RTM process parameters were measured during an actual 3D woven composite manufacturing, and used as a boundary conditions to the developed procedure. The predicted pressure inside the polymer at different length-scales was used to compute the polymer's volume fraction where the pressure was lower than the threshold below which, as shown by [112], the formation of porosities may occur. Trofimov et al. [135] did not validate predictions against experimental data.

5.1. Discussion

Accurate multi-scale solid mechanics simulations rely on the experimentally measured thermo-chemo-mechanical behavior of the polymer matrix for the range of degrees of cure and temperatures involved in the curing phase. Currently, the experimental data sets are usually limited to fully cured polymer or to very few partially cured specimens. To the best of our knowledge, there is no work dealing with the influence of the local RVE geometry on the prediction of the strain/stress development in 3D woven composites during the curing phase of the RTM process. Therefore, the required accuracy in as-woven geometry reconstruction for reliable curing phase simulations is not yet well quantified.

Interconnecting consolidation pressure and porosity requires in-situ pressure measurements

inside the composite, which has not yet been performed. Moreover, pressure measurements would help validating the numerical procedure developed by Trofimov et al. [135] which could be used in optimizing manufacturing parameters and minimizing expensive trials and errors.

6. Simulation of the cooling and demolding phase of the RTM process

Figure 11 shows a schematic representation of the demolding phase of the RTM process. Figure 11(a) details a fully solidified part being released from the mold and cooled by natural convection down to room temperature. Figure 11(b) shows a typical pressure, temperature and degree of cure evolution during the demolding phase of the RTM process. At this stage, the part is fully cured, under atmospheric pressure and it's temperature is decreasing according to the prescribed convection.

Simulating the cooling and the demolding phase is performed using the approach described in Section 5 and mainly aims at predicting residual stresses and the part's distortion.

Vasylevskyi et al. [136] compared longitudinal and transverse displacement components resulting from residual stresses build-up during the cooling of 3D woven layer-to-layer and orthogonal composites computed numerically against those measured by the hole drilling technique. Authors compared displacements around the hole cutting the weft, the warp and binder tows (for orthogonal geometry) as well the polymer matrix. For the pure polymer, Vasylevskyi et al. assumed a temperature-dependent linearly thermo-elastic constitutive model with a constant Poisson's ratio. At the micro-scale, the fibers were assumed to be distributed randomly in the polymer matrix and the thermo-mechanical properties of the tows were homogenized with an analytical micro-mechanics approach. At the meso-scale, Vasylevskyi et al. generated RVEs with non-uniform tows cross-sections using DFMA and performed cooling simulations by applying a linear temperature drop from 165°C to 25°C as a boundary condition. The simulations resulted in qualitative and, in some cases, quantitative predictions of displacement whose accuracy, mostly, increase with the distance from the hole and exhibited discrepancies smaller than 5%. The discrepancies could come from the assumption of no residual stress and strain build-up prior cooling, a simplified cooling profile, an assumed linearly elastic temperature-dependent constitutive model and local interactions of the reinforcing tows that are difficult to capture both experimentally and numerically.

Benavente et al. [117] compared the simulated and measured process-induced spring-in angle in a L-shaped layer-to-layer 3D woven composite part. For the pure polymer, the authors assumed

temperature-dependent viscoelastic mechanical models with constant Poisson's ratio while the non-mechanical behavior of the matrix was assumed to vary with temperature and degree of cure, as suggested by Svanberg et al. [115]. At the micro-scale, the fibers were assumed to have a hexagonal packing in the polymer matrix, and mechanical and non-mechanical properties were homogenized numerically and analytically, respectively. At the meso-scale, the authors used WiseTex to generate the RVE and the cooling phase was simulated by applying a temperature profile similar to Figure 11(b). A spring-in angle of 0.67° was predicted, while those usually measured experimentally under the same conditions range from 0.5° to 2°.

The multi-scale anisotropic thermo-chemo-viscoelastic approach developed by [7] (discussed in Section 5) was used to simulate distortion in a non-flat 3D woven layer-to-layer composite part exhibiting variation in properties and thickness. In the work of Trofimov et al. [7], the contoured geometry of the manufactured part was digitized using an industrial optical 3D scanner and compared against the developed multi-scale numerical predictions. It was found that the presented approach was capable of qualitative and, in some cases, quantitative prediction. For example, the relative difference between experimentally measured and predicted displacement was around $\sim 2.8\%$. It was also observed that the numerical approach was able to capture specific geometrical features as well as variations in thickness and properties of the part. The discrepancies could come from the fact that the distortion in some areas was close to the equipment sensitivity. Also, errors could be associated to an idealized RVEs at micro-and meso-scales or the effective CTE and CCS that were approximated with piecewise functions neglecting a non-linear behaviour.

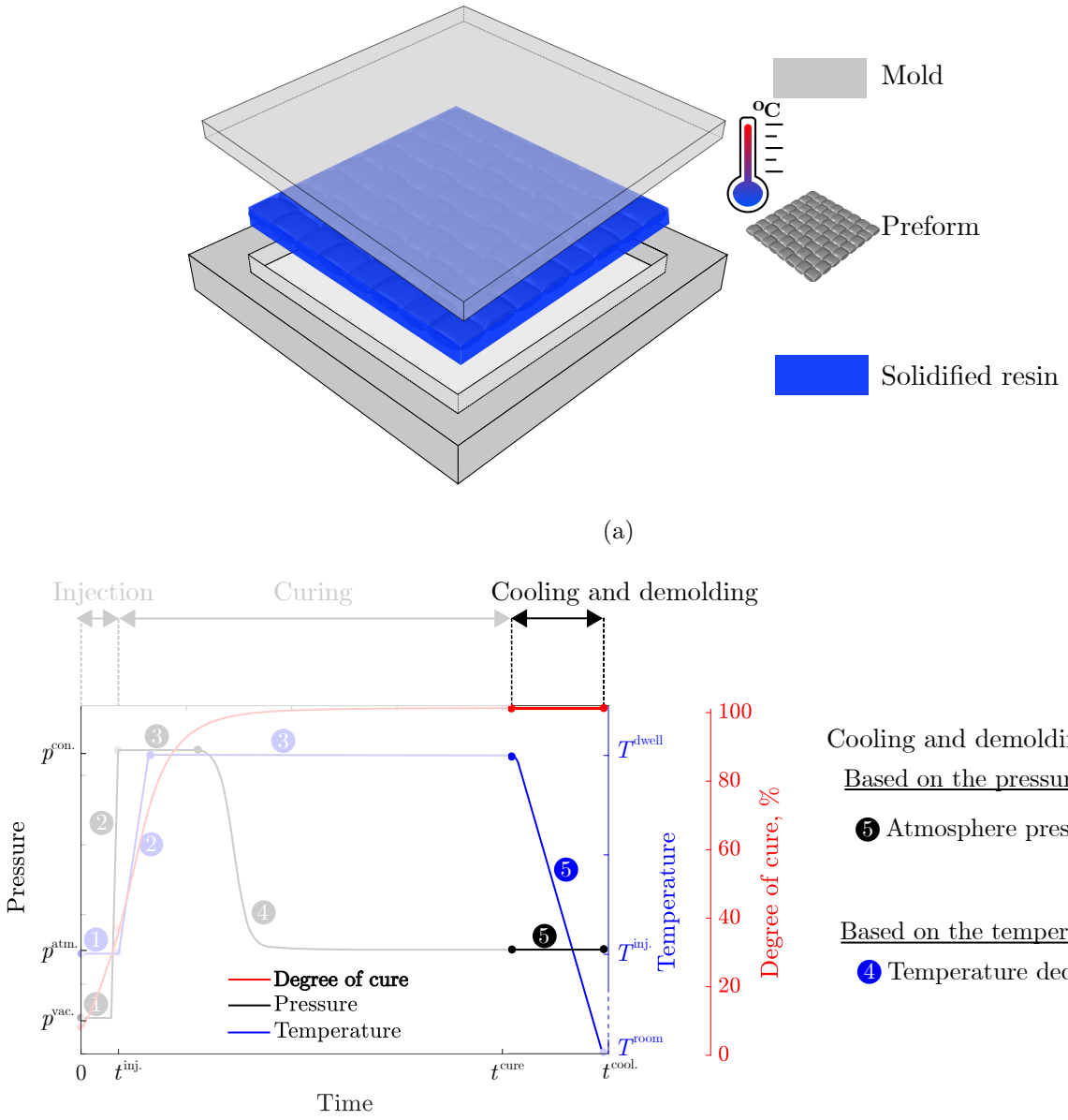

Figure 11: Schematic representation of the demolding phase of the RTM process: (a) a fully solidified part is cooled and released from the mold, led free standing and cooled by natural convection down to room temperature; (b) a typical pressure, temperature and degree of cure evolution during the demolding phase of the RTM process. At this last stage, the part is fully cured, under atmospheric pressure and the temperature is decreasing according to the prescribe convection.

6.1. Discussion

Recent studies have shown that the multi-scale simulations based on the concept of RVE are capable of predicting process induced geometrical warpage in composites with simple macro-scale geometry such as flat, L-shaped and U-shaped parts. However, one of the main advantages of the RTM process is its ability to manufacture geometrically complex parts with variable thickness and containing different fabrics. Variation in thickness may lead to a non-uniform local volume fraction of fibers inside the tows, which has not yet been addressed at length in the literature. Different fabrics would require considering multiple RVEs with transition zones, which implies that it could be of interest to validate existing approaches on more complex cases. Finally, it could be interesting to quantitatively interconnect the manufacturing parameters such as temperature cycle, etc., with the final distortion for the optimization of the RTM procedure.

7. The RTM process optimization

The research works on optimization can be grouped into the *on-line process control* that use in-situ monitoring to optimize the process during operation [137–141] and the *process design optimization* that aims at finding design parameters leading to optimal objective functions quantifying the RTM process [142, 143]. This work focuses on the latter as it benefits from the data that could be computed using approaches discussed in Sections 3, 4, 5 and 6. The works reviewing optimization algorithms and their applications to the process design optimization can be found in [144–146]. To avoid repetition of previous works, we only introduce the state of the art in the process design optimization which we then interconnect to the progress in the RTM process simulations recalled in Sections 3, 4, 5 and 6. This way we could further analyze gaps in the RTM process simulations of 3D woven composites.

Increased computational power allows research on optimizing the RTM process using multiple objectives (MO) that quantify the process more realistically than single objective (SO). An optimization with MO results in a Pareto set of solutions which are non-dominated over each other but are superior to the rest of solutions in the search space [144, 147]. The most of currently used optimization algorithms applied to the optimization of the RTM process are stochastic or evolutionary strategies and could be attributed to the zero order search methods [143, 144]. These methods start by generating a random set of solutions which they improve at each iteration using stochastic operators [143]. In zero order search methods, objective functions must be evaluated

at any point within the design space, which means that these methods are insensitive to initial conditions and avoid local minima. However, zero order search methods are computationally expensive and do not guarantee an optimum solution. The most widely used evolutionary strategies are Genetic Algorithms (GA) [148], Particle Swarm Optimisation (PSO) [149], and Ant Colony Optimisation (ACO) [150].

The problem of finding optimal design parameters such as injection ports and vents locations, injection pressure/flow rate, and temperatures of a resin and the mold that minimize injection time, mechanically entrapped air (porosity), resin rich areas and residual strain received a significant attention over the years [145, 151–158]. These works simulate an injection based on the concepts recalled in Section 4 and evaluate a MO function which is further used in an iterative search of design variables by zero order search methods resulting in a set of Pareto solutions. The MO evaluation cost might be higher than that of the search, therefore, speeding up MO evaluation include simulation simplifications assuming, for example, isotropic permeability of a preform [151] or a problem reduction from 3D to 2D or even 1D [155]. However, for the case of 3D woven preforms, such a problem simplification may result in unreliable simulations,thus most of the works consider simpler geometries such as those of 2D weaves. Due to a very limited number of works considering 3D woven preforms, we overview results for 2D preforms as well to demonstrate the state of the progress in optimizing the injection phase of the RTM. It has been reported that under isothermal conditions, an optimized number and locations of ports and vents could reduce the injection time by more than $\sim 50\%$ [156] and limit dry spots by $\sim 45\%$ [153]. The works of [144, 155] considered non-isothermal injection temperature profiles to limit the risk of flow blockage due to unwanted curing. Struzziero et al. [155] developed an approach that links FE simulations with a GA algorithm and computed the Pareto set of solutions leading to a reduction of injection time by 66% and degree of cure at the end of injection by 15%.

The problem of finding an optimal curing temperature profile and consolidation pressure that minimize residual stress, Volatile Organic Compounds (VOC), temperature overshoot, degree of cure gradients and maximize the degree of cure was discussed in [144, 159–166]. The evaluation of the MO involve solving thermomechanical problem, as discussed in Section 5 which, in general, requires significant computational resources that could be reduced by applying classical laminate theory [159], rules of mixtures [163, 165], simplified constitutive models [161] or reduce the problem from 3D to 2D [163]. In the case of 3D woven structures, the applicability of such simplifications is

limited (Section 2) and thus most of works consider laminates with less complex geometries while only one work has been found dealing with 3D woven composites [166]. Due to the very limited literature considering 3D woven preforms, we also overview results for laminates to demonstrate the state of the progress in optimizing the curing phase of the RTM process. Ruiz and Trochu [159] developed a multi-criteria optimization algorithm based on the 1D process simulation to optimize the MO function and improved a laminate composite's degree of cure, reduced residual stresses and minimized curing time. Also, the authors concluded that a more complex temperature profile is often required to appropriately cure thicker specimens. Tifkitsis et al. [160] developed a novel MO optimization method where a surrogate model is coupled with a Monte-Carlo simulator and then integrated with GA to optimize the cure process time and temperature overshoot of thick flat laminates. The optimal cure cycle computed by Tifkitsis et al. [160] was able to reduce the cure time and maximum overshoot temperature by $\sim 40\%$, as compared to standard solutions whilst reducing variability by about $\sim 20\%$. Struzziero et al. [163] developed a procedure that combines the FE simulation of the heat transfer and a GA to minimize the curing time and temperature overshoot. For ultra-thick components (60 mm and above), Struzziero et al. [163] reported a reduction of curing time and temperature overshoot by 14 h and 70%, respectively. For thick components (24 mm), Struzziero et al. [163] reported a reduction of curing time and temperature overshoot by 50% for both. Dolkun et al. [165] developed an approach combining 2D FE thermal simulations and a GA algorithm to minimize gradients of degree of cure and temperature as well as the curing time of a 24 mm thick unidirectional laminate. The optimized cure profile reduced gradients of degree of cure and temperature by $\sim 56\%$ and $\sim 71\%$, respectively, as well as curing time by $\sim 33\%$. Wang et al. [166] used a multi-scale simulation procedure (see Section 5 for more details) to develop a computationally efficient surrogate model based on the radial basis function which was then used in a GA driven MO optimization. The authors reported that minimizing residual stresses requires longer curing time, therefore, the maximum reduction of residual stresses ($\sim 42\%$) minimizes the curing time by $\sim 32\%$, as compared to the manufacturer suggested parameters. Simultaneously, the maximum reduction of curing time ($\sim 80\%$) minimizes the residual stress by $\sim 2\%$. Hui et al. [164] developed an optimization algorithm that combines FE process simulations with a non-dominated sorting GA (NSGA-II) to reduce the maximum temperature gradient, the maximum residual stress and the process time in composite laminates. The authors reported an optimized cure cycle that reduces the curing time by $\sim 20\%$, the temperature gradient by $\sim 42\%$ and the residual stress by

Table 1: Summary of the selected multi-scale simulation results of the RTM process

Phase of the RTM	Predicted quantity	Models description					Accuracy	Suggestions	Refs
		Constit. model	Micro geom.	Meso geom.	Micro simul.	Meso simul.			
Injection	Permeability	Stokes, Darcy	Hexag. Square Rand.	Layer-to-layer Orthogonal	Analyt. and Numeric.	Numeric.	Qualit.	Standardization of experiments Standardization of simulations Increase meso-RVE fidelity Sensistivity study	[27] [90] [92] [95]
Curing	Residual strain	Thermo-chemo-elastic Thermo-chemo-viscoelastic constant Poisson's ratio	Hexag. Square Rand.	Layer-to-layer Orthogonal	Analyt. and numeric.	Numeric.	Qualit.	Detailed resin character. Sensitivity study	[122] [123] [134] [7] [135]
Cooling and demolding	Spring-in angle Residual stress Displacement	Thermo-chemo-elastic Thermo-chemo-viscoelastic constant Poisson's ratio	Hexag. Square Rand.	Layer-to-layer Through thickness Orthogonal	Analyt. and numeric.	Numeric.	Quantit.	More complex part' geometries Parts made of different fabrics Sensitivity study	[117] [136] [7]

$\sim 20\%$, as compared to the manufacturer recommended curing cycle.

To the best of our knowledge, the problem of finding optimal cooling rate and demolding time that minimize residual stress has never been addressed separately. Instead, finding optimal cooling rate is usually included in the curing optimization [164, 166] while optimization of the demolding time has never been addressed so far. The optimal demolding time could limit cases when the part gets stuck in the mold and reduce extra manual work.

7.1. Discussion

Recent studies have shown that the main problem in optimizing the RTM process applied to 3D woven composites is the MO evaluation cost which is much higher than that of the search. Currently, reduction of the MO evaluation cost is achieved by considering, for example, idealized micro-and meso-structures, problem reduction from a 3D to a 2D or a 1D and simplified constitutive model. However, such simplifications are not capable of capturing the complex nature of 3D woven composites and, therefore, a very limited number of works consider 3D woven structures. Building surrogate models requires a sensitivity analysis aiming at the identification of the critical model parameters that need to be included. Given the current progress in the field of machine learning and artificial intelligence, physics informed neural networks could be used to develop robust and efficient surrogate models for process simulations as discussed in [167, 168].

8. Concluding remarks, challenges, and future opportunities

This work shows that the concept of an RVE and the homogenization procedure have been widely used with different level of success to develop numerical tools simulating the RTM process, as summarized in Table 1. It has been reported that a robust constitutive model of a polymer

Table 2: Summary of the progress in optimizing the RTM process

Stage of the RTM process	Design parameter	Objective functions	Main achievements	Main limitations	Suggestions	Refs
Injection	Number and location of injection ports and vents Injection pressure or flow rate Injection temperature profile Mold temperature	Min. Injection time Min. pores Min. resin rich areas Min. strain level	Reduction of injection time Reduction of porosity Reduction of pressure	The MO evaluation cost is much higher than that of the search Standardize permeability measurements Lack of a standardized permeability measurements Lack of a standardized permeability predictions	Identify critical micro-and meso-scale parameters of the simulation models AI simulation of the process	[151–158]
Curing	Curing temperature Curing time Cooling temperature Cooling time Consolidation pressure	Min. residual stress Min. VOC Min. degree of cure gradients Max. degree of cure	Reduction of residual stress The thicker part the more complex curing is required Reduction of the temperature overshoot Reduction of cure time	The MO evaluation cost is much higher than that of the search Limited works on the effect of consolidation pressure	Identify critical micro-and meso-scale parameters of the simulation models AI simulation of the process	[144, 159–165]
Cooling and demolding	Cooling rate Demolding time	Min. residual stress	Reduction of residual stress	The MO evaluation cost is much higher than that of the search	Identify critical micro-and meso-scale parameters of the simulation models	[164, 166]

valid at all ranges of degrees of cure and temperatures involved in the RTM process, a realistic representation of composites at micro- and meso-scales are a key for accurate process simulation.

However, it has been shown that studies on the RTM process optimization, summarized in the Table 2, widely rely on simplified simulations and rarely benefit from recent developments due to their high computational costs. Therefore, finding a trade-off between accuracy and computational efficiency is required for further progress in the process optimization.

Below we summarize possible actions that could help improving the accuracy of the RTM simulations and increase the use of recent numerical tools in the process optimization.

Action 1: Develop polymer constitutive models databases that rely on the experimental data at all ranges of degrees of cure and temperatures involved in the process. Currently, most of the works use experimental data for a fully cured or a very few partially cured specimens because measurements at low degrees of cure and temperatures above T_g present a serious challenge.

Action 2: Verify the accuracy of simulation tools on complex parts made of different preform types. Currently, most of the simulation efforts are dedicated to simple geometries of composite parts neglecting RTM advantage of manufacturing complex shaped parts exhibiting variation in thickness and properties. It could be of interest to test developed models on the part containing different types of fabrics and non-uniform thickness.

Action 3: Increase computational efficiency of degree of cure- and temperature-dependent viscoelastic constitutive models accounting for the stress relaxation. Currently, degree of cure- and temperature-dependent viscoelastic models require up to 30 times more computational time than their thermo-elastic counterparts that have limited range of applicability as they neglect viscoelastic effects.

Action 4: Increase computational efficiency of the multi-scale homogenization procedure. This work requires performing sensitivity analysis resulting in a limited set of critical

problem-specific micro-and meso-structural. Limiting a set of parameters could help simplifying the simulation procedure with a predicted level of accuracy. The set of parameters may include tows geometry and their cross-sections, local volume fraction of fibers inside tows and gaps between the tows. Thanks to recent advances in image processing, experimentally observed structures could be transferred into numerical representations serving as a reference. Moreover, substituting FE simulations with that using the Fast Fourier Transform software such as Amitex [169] or Craft [170] could increase computational efficiency.

Action 5: Standardize experimental measurements and numerical approaches. Currently, measurements related to injection and curing phases require additional work on guidelines while measurements of process-induced distortions are more standardized. Standardized measurements could help in the sensitivity analysis (Action 4) building experimentally validated reference simulations. Similarly, numerical simulations of injection and curing phases require extra work on the development of robust guidelines limiting unnecessary numerical errors associated with meshing, boundary conditions, and the digitization of RVEs.

9. Acknowledgment

We acknowledge the support of Safran S.A., and the the Natural Sciences and Engineering Research Council of Canada (NSERC) (CRDPJ514761-17)

References

[1] GE Aviation. 3

[2] B. Liu, S. Bickerton, S. G. Advani, Modelling and simulation of resin transfer moulding (RTM) - Gate control, venting and dry spot prediction, Composites Part A: Applied Science and Manufacturing 27 (2) (1996) 135–141. doi:10.1016/1359-835X(95)00012-Q. 2, 12

[3] E. Ruiz, F. Trochu, Numerical analysis of cure temperature and internal stresses in thin and thick RTM parts, Composites Part A: Applied Science and Manufacturing 36 (6) (2005) 806–826. doi:10.1016/j.compositesa.2004.10.021.

[4] M. Benavente, L. Marcin, A. Courtois, M. Lévesque, E. Ruiz, Numerical analysis of viscoelastic process-induced residual distortions during manufacturing and post-curing, Composites Part A: Applied Science and Manufacturing 107 (2018) 205–216. doi:10.1016/j.compositesa.2018.01.005. 2, 18, 19

[5] P. Boisse, Advances in composites manufacturing and process design, Woodhead Publishing, 2015. 2, 3

[6] V. V. Vasiliev, E. Morozov, Advanced Mechanics of Composite Materials., Elsevier, 2007. 2, 3

[7] A. Trofimov, J. Le-Pavic, C. Ravey, W. Albouy, D. Therriault, M. Lévesque, Multi-scale modeling of distortion in the non-flat 3D woven composite part manufactured using Resin Transfer Molding, Composites Part A: Applied Science and Manufacturing (2020) 106145doi:10.1016/j.compositesa.2020.106145. 2, 4, 16, 17, 19, 20, 22, 27

[8] B. Widom, Random Sequential Addition of Hard Spheres to a Volume, The Journal of Chemical Physics 44 (10) (1966) 3888–3894. doi:10.1063/1.1726548. 2, 11

[9] J. L. Finney, Fine structure in randomly packed, dense clusters of hard spheres, Materials Science and Engineering 23 (2-3) (1976) 199–205. doi:10.1016/0025-5416(76)90194-4.

[10] D. He, N. Ekere, L. Cai, Computer simulation of random packing of unequal particles, Physical Review E 60 (6) (1999) 7098–7104. doi:10.1103/PhysRevE.60.7098.

[11] A. Trofimov, B. Drach, I. Sevostianov, Effective elastic properties of composites with particles of polyhedral shapes, International Journal of Solids and Structures 120 (2017) 157–170. doi:10.1016/j.ijsolstr.2017.04.037. 2, 11

[12] F. Stig, S. Hallström, Spatial modelling of 3D-woven textiles, Composite Structures 94 (5) (2012) 1495–1502. doi:10.1016/J.COMPSTRUCT.2011.12.003. 2

[13] Z. Yang, W. Ren, R. Sharma, S. McDonald, M. Mostafavi, Y. Vertyagina, T. Marrow, In-situ X-ray computed tomography characterisation of 3D fracture evolution and image-based numerical homogenisation of concrete, Cement and Concrete Composites 75 (2017) 74–83. doi:10.1016/j.cemconcomp.2016.10.001.

[14] A. Trofimov, T. Mishurova, L. Lanzoni, E. Radi, G. Bruno, I. Sevostianov, Microstructural analysis and mechanical properties of concrete reinforced with polymer short fibers, International Journal of Engineering Science 133 (2018) 210–218. doi:10.1016/J.IJENGSCI.2018.09.009. 2

[15] R. Hill, Elastic Properties of Reinforced Solids: Some Theoritical Principles (1963). doi:10.1016/0022-5096(63)90036-X. 3

[16] E. Kröner, Statistical Continuum Mechanics, Vol. 92 of CISM International Centre for Mechanical Sciences, Springer Vienna, Vienna, 1971. doi:10.1007/978-3-7091-2862-6. 3

[17] T. Mori, K. Tanaka, Average stress in matrix and average elastic energy of materials with misfitting inclusions, Acta Metallurgica 21 (5) (1973) 571–574. doi:10.1016/0001-6160(73)90064-3. 4

[18] A. A. Gusev, Representative volume element size for elastic composites: A numerical study, Journal of the Mechanics and Physics of Solids 45 (9) (1997) 1449–1459. doi:10.1016/S0022-5096(97)00016-1. 4, 11

[19] K. Terada, M. Hori, T. Kyoya, N. Kikuchi, Simulation of the multi-scale convergence in computational homogenization approaches, International Journal of Solids and Structures 37 (16) (2000) 2285–2311. doi:10.1016/S0020-7683(98)00341-2.

[20] J. Segurado, J. Llorca, A numerical approximation to the elastic properties of sphere-reinforced composites, Journal of the Mechanics and Physics of Solids 50 (10) (2002) 2107–2121. doi:10.1016/S0022-5096(02)00021-2. 4

[21] C. Karch, Micromechanical Analysis of Thermal Expansion Coefficients, Modeling and Numerical Simulation of Material Science 04 (03) (2014) 104–118. doi:10.4236/mnsms.2014.43012. 4

[22] V. Levin, On the coefficients of thermal expansion of heterogeneous material, Mekhanika Tverdogo Tela 2 (1967) 58–61. 4

[23] A. Trofimov, J. Le-Pavic, D. Therriault, M. Lévesque, An efficient multi-scale computation of the macroscopic coefficient of thermal expansion: Application to the Resin Transfer Molding manufactured 3D woven composites, International Journal of Solids and Structures 210-211 (2021) 162–169. doi:10.1016/j.ijsolstr.2020.11.012. 4

[24] F.-J. U. Luc Dormieux, Djimédo Kondo, Microporomechanics, John Wiley & Sons, 2006. 4

[25] T. Tran, S. Comas-Cardona, N.-E. Abriak, C. Binetruy, Unified microporomechanical approach for mechanical behavior and permeability of misaligned unidirectional fiber reinforcement, Composites Science and Technology 70 (9) (2010) 1410–1418. doi:10.1016/j.compscitech.2010.04.023.
URL https://linkinghub.elsevier.com/retrieve/pii/S0266353810001685 4

[26] E. Lopez, E. Abisset-Chavanne, F. Lebel, R. Upadhyay, S. Comas, C. Binetruy, F. Chinesta, Flow modeling of linear and nonlinear fluids in two and three scale fibrous fabrics, International Journal of Material Forming 9 (2) (2016) 215–227. doi:10.1007/s12289-015-1224-0.
URL http://link.springer.com/10.1007/s12289-015-1224-0 4

[27] M. Karaki, A. Hallal, R. Younes, F. Trochu, P. Lafon, A. Hayek, A. Kobeissy, A. Fayad, A comparative analytical, numerical and experimental analysis of the microscopic permeability of fiber bundles in composite materials, International Journal of Composite Materials 7 (3) (2017) 82–102. doi:10.5923/j.cmaterials.20170703.02. 4, 13, 14, 27

[28] M. Klitz, Homogenised Fluid Flow Equations in Porous Media with Application to Permeabil-

ity Computations in Textiles, Ph.D. thesis, Rheinische Friedrich-Wilhelms-University Bonn (2006). 5, 13

[29] D. A. Edwards, M. Shapiro, P. Bar-Yoseph, M. Shapira, The influence of Reynolds number upon the apparent permeability of spatially periodic arrays of cylinders, Physics of Fluids A 2 (1) (1990) 45–55. doi:10.1063/1.857691. 5

[30] K. A. Khan, A. H. Muliana, Effective thermal properties of viscoelastic composites having field-dependent constituent properties, Acta Mech 209 (2010) 153–178. doi:10.1007/s00707-009-0171-6. 5

[31] M. A. F. Zarandi, S. Arroyo, K. M. Pillai, Longitudinal and transverse flows in fiber tows: Evaluation of theoretical permeability models through numerical predictions and experimental measurements, Composites Part A: Applied Science and Manufacturing 119 (2019) 73–87. doi:10.1016/j.compositesa.2018.12.032. 5, 13, 14

[32] A. Hallal, R. Younes, F. Fardoun, Review and comparative study of analytical modeling for the elastic properties of textile composites, Composites Part B: Engineering 50 (2013) 22–31. doi:10.1016/j.compositesb.2013.01.024. 5

[33] B. Drach, D. Kuksenko, I. Sevostianov, Effect of a curved fiber on the overall material stiffness, International Journal of Solids and Structures 100-101 (2016) 211–222. doi:10.1016/j.ijsolstr.2016.08.018. 5

[34] X. Chen, P. Potiyaraj, CAD/CAM of Orthogonal and Angle-Interlock Woven Structures for Industrial Applications, Textile Research Journal 69 (9) (1999) 648–655. doi:10.1177/004051759906900905. 5

[35] K. Bilisik, Multiaxis three-dimensional weaving for composites: A review, Textile Research Journal 82 (7) (2012) 725–743. doi:10.1177/0040517511435013.

[36] D. Durville, I. Baydoun, H. Moustacas, G. Périé, Y. Wielhorski, Determining the initial configuration and characterizing the mechanical properties of 3D angle-interlock fabrics using finite element simulation, International Journal of Solids and Structures 154 (2018) 97–103. doi:10.1016/j.ijsolstr.2017.06.026. 5

[37] B. El Said, D. Ivanov, A. C. Long, S. R. Hallett, Multi-scale modelling of strongly heterogeneous 3D composite structures using spatial Voronoi tessellation, Journal of the Mechanics and Physics of Solids 88 (2016) 50–71. doi:10.1016/j.jmps.2015.12.024. 6

[38] A. Geoffre, Y. Wielhorski, N. Moulin, J. Bruchon, S. Drapier, P. J. Liotier, Influence of intra-yarn flows on whole 3D woven fabric numerical permeability: from Stokes to Stokes-Darcy simulations, International Journal of Multiphase Flow 129 (2020). doi:10.1016/j.ijmultiphaseflow.2020.103349. 6

[39] Y. Wielhorski, A. Mendoza, M. Rubino, S. Roux, Numerical modeling of 3D woven composite reinforcements: A review, Composites Part A: Applied Science and Manufacturing 154 (November 2021) (2022) 106729. doi:10.1016/j.compositesa.2021.106729. 6

[40] T. Gereke, C. Cherif, A review of numerical models for 3D woven composite reinforcements, Composite Structures 209 (July 2018) (2019) 60–66. doi:10.1016/j.compstruct.2018.10.085. 6

[41] Y. Miao, E. Zhou, Y. Wang, B. A. Cheeseman, Mechanics of textile composites: Micro-geometry, Composites Science and Technology 68 (7-8) (2008) 1671–1678. doi:10.1016/j.compscitech.2008.02.018. 6

[42] J. Bonet, A. Burton, A simple orthotropic, transversely isotropic hyperelastic constitutive equation for large strain computations, Computer Methods in Applied Mechanics and Engineering 162 (1-4) (1998) 151–164. doi:10.1016/S0045-7825(97)00339-3. 6

[43] A. Charmetant, E. Vidal-Sallé, P. Boisse, Hyperelastic modelling for mesoscopic analyses of composite reinforcements, Composites Science and Technology 71 (14) (2011) 1623–1631. doi:10.1016/j.compscitech.2011.07.004. 6

[44] H. Xiao, O. T. Bruhns, A. Meyers, Hypo-Elasticity Model Based upon the Logarithmic Stress Rate, Journal of Elasticity 47 (1) (1997) 51–68. doi:10.1023/A:1007356925912. 6

[45] X. Peng, J. Cao, A continuum mechanics-based non-orthogonal constitutive model for woven composite fabrics, Composites Part A: Applied Science and Manufacturing 36 (6) (2005) 859–874. doi:10.1016/j.compositesa.2004.08.008.

[46] P. Boisse, Finite element analysis of composite forming, in: Composites Forming Technologies, Elsevier, 2007, pp. 46–79. doi:10.1533/9781845692537.46. 6

[47] A. Long, L. Brown, Modelling the geometry of textile reinforcements for composites: TexGen, in: Composite Reinforcements for Optimum Performance, no. 2007, Elsevier, 2011, pp. 239–264. doi:10.1533/9780857093714.2.239. 6

[48] H. Lin, X. Zeng, M. Sherburn, A. C. Long, M. J. Clifford, Automated geometric modelling of textile structures, Textile Research Journal 82 (16) (2012) 1689–1702. doi:10.1177/0040517511418562. 6

[49] I. Verpoest, S. V. Lomov, Virtual textile composites software WiseTex: Integration with micro-mechanical, permeability and structural analysis, Composites Science and Technology 65 (15-16 SPEC. ISS.) (2005) 2563–2574. doi:10.1016/j.compscitech.2005.05.031. 6

[50] A. Doitrand, C. Fagiano, F. X. Irisarri, M. Hirsekorn, Comparison between voxel and consistent meso-scale models of woven composites, Composites Part A: Applied Science and Manufacturing 73 (2015) 143–154. doi:10.1016/j.compositesa.2015.02.022. 7

[51] Y. Wang, X. Sun, Digital-element simulation of textile processes, Composites Science and Technology 61 (2) (2001) 311–319. doi:10.1016/S0266-3538(00)00223-2. 7

[52] G. Zhou, X. Sun, Y. Wang, Multi-chain digital element analysis in textile mechanics, Composites Science and Technology 64 (2) (2004) 239–244. doi:10.1016/S0266-3538(03)00258-6. 7

[53] B. Drach, I. Tsukrov, A. Trofimov, T. Gross, A. Drach, Comparison of stress-based failure criteria for prediction of curing induced damage in 3D woven composites, Composite Structures 189 (April 2017) (2018) 366–377. doi:10.1016/j.compstruct.2018.01.057. 7

[54] B. Jähne (Ed.), Spatio-Temporal Image Processing, Vol. 751 of Lecture Notes in Computer Science, Springer Berlin Heidelberg, Berlin, Heidelberg, 1993. doi:10.1007/3-540-57418-2. 8

[55] I. Straumit, S. V. Lomov, M. Wevers, Quantification of the internal structure and automatic generation of voxel models of textile composites from X-ray computed tomography data,

Composites Part A: Applied Science and Manufacturing 69 (2015) 150–158. doi:10.1016/j.compositesa.2014.11.016. 8

[56] Y. Liu, I. Straumit, D. Vasiukov, S. V. Lomov, S. Panier, Prediction of linear and non-linear behavior of 3D woven composite using mesoscopic voxel models reconstructed from X-ray micro-tomography, Composite Structures 179 (2017) 568–579. doi:10.1016/j.compstruct.2017.07.066. 8, 9

[57] A. Mendoza, R. Trullo, Y. Wielhorski, Descriptive modeling of textiles using FE simulations and deep learning, Composites Science and Technology 213 (June) (2021) 108897. arXiv:2106.13982, doi:10.1016/j.compscitech.2021.108897. 9, 10

[58] M. A. Ali, Q. Guan, R. Umer, W. J. Cantwell, T. J. Zhang, Deep learning based semantic segmentation of µCT images for creating digital material twins of fibrous reinforcements, Composites Part A: Applied Science and Manufacturing 139 (June) (2020) 106131. doi:10.1016/j.compositesa.2020.106131. 9

[59] Y. Huang, K. K. Jin, S. K. Ha, Effects of fiber arrangement on mechanical behavior of unidirectional composites, Journal of Composite Materials 42 (18) (2008) 1851–1871. doi:10.1177/0021998308093910. 10, 11

[60] J. Seuffert, L. Bittrich, L. Cardoso de Oliveira, A. Spickenheuer, L. Kärger, Micro-Scale Permeability Characterization of Carbon Fiber Composites Using Micrograph Volume Elements, Frontiers in Materials 8 (2021) 428. doi:10.3389/FMATS.2021.745084/BIBTEX. 10

[61] M. Karahan, S. V. Lomov, A. E. Bogdanovich, D. Mungalov, I. Verpoest, Internal geometry evaluation of non-crimp 3D orthogonal woven carbon fabric composite, Composites Part A: Applied Science and Manufacturing 41 (9) (2010) 1301–1311. doi:10.1016/j.compositesa.2010.05.014. 10

[62] S.-M. Park, J. H. Lim, M. R. Seong, D. Sohn, Efficient generator of random fiber distribution with diverse volume fractions by random fiber removal, Composites Part B: Engineering 167 (2019) 302–316. doi:10.1016/j.compositesb.2018.12.042. 11, 12

[63] S. Li, General unit cells for micromechanical analyses of unidirectional composites, Com-

posites - Part A: Applied Science and Manufacturing 32 (6) (2001) 815–826. doi:10.1016/S1359-835X(00)00182-2. 11

[64] B. D. Lubachevsky, F. H. Stillinger, Geometric properties of random disk packings, Journal of Statistical Physics 60 (5-6) (1990) 561–583. doi:10.1007/BF01025983. 11

[65] A. Donev, S. Torquato, F. H. Stillinger, Neighbor list collision-driven molecular dynamics simulation for nonspherical hard particles. I. Algorithmic details, Journal of Computational Physics 202 (2) (2005) 737–764. doi:10.1016/j.jcp.2004.08.014.

[66] E. Ghossein, M. Lévesque, Random generation of periodic hard ellipsoids based on molecular dynamics: A computationally-efficient algorithm, Journal of Computational Physics 253 (2013) 471–490. doi:10.1016/j.jcp.2013.07.004. 11

[67] M. D. Rintoul, S. Torquato, Reconstruction of the Structure of Dispersions, Journal of Colloid and Interface Science 186 (2) (1997) 467–476. doi:10.1006/jcis.1996.4675. 11

[68] L. Yang, Y. Yan, Z. Ran, Y. Liu, A new method for generating random fibre distributions for fibre reinforced composites, Composites Science and Technology 76 (2013) 14–20. doi:10.1016/j.compscitech.2012.12.001. 11

[69] J. Bénézech, G. Couégnat, Variational segmentation of textile composite preforms from X-ray computed tomography, Composite Structures 230 (2019) 111496. doi:10.1016/j.compstruct.2019.111496. 12

[70] F. Trochu, E. Ruiz, V. Achim, S. Soukane, Advanced numerical simulation of liquid composite molding for process analysis and optimization, Composites Part A: Applied Science and Manufacturing 37 (6 SPEC. ISS.) (2006) 890–902. doi:10.1016/j.compositesa.2005.06.003. 12

[71] P. Šimáček, S. G. Advani, Desirable features in mold filling simulations for liquid composite molding processes, Polymer Composites 25 (4) (2004) 355–367. doi:10.1002/pc.20029.

[72] A. Koorevaar, Simulation of Liquid Injection Moulding, in: Proceedings of SAMPE 2002, Paris, 2002.

[73] H. G. Weller, G. Tabor, H. Jasak, C. Fureby, A tensorial approach to computational continuum mechanics using object-oriented techniques, Computers in Physics 12 (6) (1998) 620. doi:10.1063/1.168744. 12

[74] T. S. Lundström, B. R. Gebart, Effect of Perturbation of Fibre Architecture on Permeability Inside Fibre Tows, Journal of Composite Materials 29 (4) (1995) 424–443. doi:10.1177/002199839502900401. 13

[75] K. M. Pillai, S. G. Advani, Numerical and analytical study to estimate the effect of two length scales upon the permeability of a fibrous porous medium, Transport in Porous Media 21 (1) (1995) 1–17. doi:10.1007/BF00615332. 13

[76] G. Allaire, Homogenization of the stokes flow in a connected porous medium, Asymptotic Analysis 2 (3) (1989) 203–222. doi:10.3233/ASY-1989-2302. 13

[77] P. Angot, C. H. Bruneau, P. Fabrie, A penalization method to take into account obstacles in incompressible viscous flows, Numerische Mathematik 81 (4) (1999) 497–520. doi:10.1007/s002110050401.

[78] P. Angot, Analysis of singular perturbations on the Brinkman problem for fictitious domain models of viscous flows, Mathematical Methods in the Applied Sciences 22 (16) (1999) 1395–1412. doi:10.1002/(SICI)1099-1476(19991110)22:16<1395::AID-MMA84>3.0.CO;2-3. 13

[79] A. Tamayol, M. Bahrami, Transverse permeability of fibrous porous media, PHYSICAL REVIEW E 83 (2011) 46314. doi:10.1103/PhysRevE.83.046314. 13

[80] Z. Cai, A. L. Berdichevsky, An improved self-consistent method for estimating the permeability of a fiber assembly, Polymer Composites 14 (4) (1993) 314–323. doi:10.1002/PC.750140407. 13

[81] B. R. Gebart, Permeability of Unidirectional Reinforcements for RTM, Journal of Composite Materials 26 (8) (1992) 1100–1133. doi:10.1177/002199839202600802. 13

[82] J. Drummond, M. Tahir, Laminar viscous flow through regular arrays of parallel solid cylinders, International Journal of Multiphase Flow 10 (5) (1984) 515–540. doi:10.1016/0301-9322(84)90079-X. 13

[83] S. Kuwabara, The Forces experienced by Randomly Distributed Parallel Circular Cylinders or Spheres in a Viscous Flow at Small Reynolds Numbers, Journal of the Physical Society of Japan 14 (4) (1959) 527–532. doi:10.1143/JPSJ.14.527. 13

[84] J. Van der Westhuizen, J. Prieur Du Plessis, An attempt to quantify fibre bed permeability utilizing the phase average Navier-Stokes equation, Composites Part A: Applied Science and Manufacturing 27 (4) (1996) 263–269. doi:10.1016/1359-835X(95)00039-5.
URL https://linkinghub.elsevier.com/retrieve/pii/1359835X95000395 14

[85] M. V. Bruschke, S. G. Advani, Flow of generalized Newtonian fluids across a periodic array of cylinders, Journal of Rheology 37 (3) (1993) 479–498. doi:10.1122/1.550455. 14

[86] M. Bodaghi, S. V. Lomov, P. Simacek, N. C. Correia, S. G. Advani, On the variability of permeability induced by reinforcement distortions and dual scale flow in liquid composite moulding: A review, Composites Part A: Applied Science and Manufacturing 120 (2019) 188–210. doi:10.1016/J.COMPOSITESA.2019.03.004. 14

[87] B. Verleye, R. Croce, M. Griebel, M. Klitz, S. V. Lomov, G. Morren, H. Sol, I. Verpoest, D. Roose, Permeability of textile reinforcements: Simulation, influence of shear and validation, Composites Science and Technology 68 (13) (2008) 2804–2810. doi:10.1016/j.compscitech.2008.06.010. 14

[88] F. Loix, P. Badel, L. Orgéas, C. Geindreau, P. Boisse, Woven fabric permeability: From textile deformation to fluid flow mesoscale simulations, Composites Science and Technology 68 (7-8) (2008) 1624–1630. doi:10.1016/J.COMPSCITECH.2008.02.027.

[89] Z. R. Chen, L. Ye, M. Lu, Permeability predictions for woven fabric preforms, Journal of Composite Materials 44 (13) (2010) 1569–1586. doi:10.1177/0021998309355888. 14

[90] E. E. Swery, R. Meier, S. V. Lomov, K. Drechsler, P. Kelly, Predicting permeability based on flow simulations and textile modelling techniques: Comparison with experimental values and verification of FlowTex solver using Ansys CFX, Journal of Composite Materials 50 (5) (2016) 601–615. doi:10.1177/0021998315579927. 14, 27

[91] N. Vernet, E. Ruiz, S. Advani, J. B. Alms, M. Aubert, M. Barburski, B. Barari, J. M. Beraud, D. C. Berg, N. Correia, M. Danzi, T. Delavière, M. Dickert, C. Di Fratta, A. Endruweit,

P. Ermanni, G. Francucci, J. A. Garcia, A. George, C. Hahn, F. Klunker, S. V. Lomov, A. Long, B. Louis, J. Maldonado, R. Meier, V. Michaud, H. Perrin, K. Pillai, E. Rodriguez, F. Trochu, S. Verheyden, M. Weitgrefe, W. Xiong, S. Zaremba, G. Ziegmann, Experimental determination of the permeability of engineering textiles: Benchmark II, Composites Part A: Applied Science and Manufacturing 61 (2014) 172–184. doi:10.1016/j.compositesa.2014.02.010. 14, 16

[92] E. E. Swery, T. Allen, P. Kelly, Capturing the influence of geometric variations on permeability using a numerical permeability prediction tool, Journal of Reinforced Plastics and Composites 35 (24) (2016) 1802–1813. doi:10.1177/0731684416669249. 14, 16, 27

[93] M. Ali, R. Umer, K. Khan, S. Bickerton, W. Cantwell, Non-destructive evaluation of through-thickness permeability in 3D woven fabrics for composite fan blade applications, Aerospace Science and Technology 82-83 (2018) 520–533. doi:10.1016/j.ast.2018.10.003. 14, 15

[94] H. Alhussein, R. Umer, S. Rao, E. Swery, S. Bickerton, W. J. Cantwell, Characterization of 3D woven reinforcements for liquid composite molding processes, Journal of Materials Science 51 (6) (2016) 3277–3288. doi:10.1007/s10853-015-9640-6. 14, 15

[95] M. A. Ali, R. Umer, K. A. Khan, W. J. Cantwell, In-plane virtual permeability characterization of 3D woven fabrics using a hybrid experimental and numerical approach, Composites Science and Technology 173 (August 2018) (2019) 99–109. doi:10.1016/j.compscitech.2019.01.030. 15, 27

[96] M. Ali, R. Umer, K. Khan, W. Cantwell, XCT-scan assisted flow path analysis and permeability prediction of a 3D woven fabric, Composites Part B: Engineering 176 (2019) 107320. doi:10.1016/j.compositesb.2019.107320. 15

[97] M. Bodaghi, A. Vanaerschot, S. V. Lomov, N. C. Correia, On the variability of mesoscale permeability of a 2/2 twill carbon fabric induced by variability of the internal geometry, Composites Part A: Applied Science and Manufacturing 101 (2017) 394–407. doi:10.1016/j.compositesa.2017.05.030. 16

[98] D. May, E. Syerko, T. Schmidt, C. Binetruy, L. R. da Silva, S. Lomov, S. Advani, Benchmarking virtual permeability predictions of real fibrous microstructure, in: 36th Technical Conference of the American Society for Composites 2021: Composites Ingenuity Taking on Challenges in

Environment-Energy-Economy, ASC 2021, Vol. 3, DEStech Publications, 2021, pp. 2123–2132. doi:10.12783/asc36/35901. 16

[99] E. Syerko, T. Schmidt, D. May, C. Binetruy, S. Advani, S. Lomov, L. Silva, S. Abaimov, N. Aissa, I. Akhatov, M. Ali, N. Asiaban, G. Broggi, J. Bruchon, B. Caglar, H. Digonnet, J. Dittmann, S. Drapier, A. Endruweit, A. Guilloux, R. Kandinskii, A. Leygue, B. Mahato, P. Martínez-Lera, M. Matveev, V. Michaud, P. Middendorf, N. Moulin, L. Orgéas, C. Park, S. Rief, M. Rouhi, I. Sergeichev, M. Shakoor, O. Shishkina, Y. Swolfs, M. Tahani, R. Umer, K. Vanclooster, R. Vorobyev, Benchmark exercise on image-based permeability determination of engineering textiles: Microscale predictions, Composites Part A: Applied Science and Manufacturing 167 (2023) 107397. doi:10.1016/J.COMPOSITESA.2022.107397. 16

[100] C. Demaría, E. Ruiz, F. Trochu, In-plane anisotropic permeability characterization of deformed woven fabrics by unidirectional injection. Part I: Experimental results, Polymer Composites 28 (6) (2007) 797–811. doi:10.1002/pc.20107. 16

[101] D. May, A. Aktas, S. G. Advani, D. C. Berg, A. Endruweit, E. Fauster, S. V. Lomov, A. Long, P. Mitschang, S. Abaimov, D. Abliz, I. Akhatov, M. A. Ali, T. D. Allen, S. Bickerton, M. Bodaghi, B. Caglar, H. Caglar, A. Chiminelli, N. Correia, B. Cosson, M. Danzi, J. Dittmann, P. Ermanni, G. Francucci, A. George, V. Grishaev, M. Hancioglu, M. A. Kabachi, K. Kind, M. Deléglise-Lagardère, M. Laspalas, O. V. Lebedev, M. Lizaranzu, P. J. Liotier, P. Middendorf, J. Morán, C. H. Park, R. B. Pipes, M. F. Pucci, J. Raynal, E. S. Rodriguez, R. Schledjewski, R. Schubnel, N. Sharp, G. Sims, E. M. Sozer, P. Sousa, J. Thomas, R. Umer, W. Wijaya, B. Willenbacher, A. Yong, S. Zaremba, G. Ziegmann, In-plane permeability characterization of engineering textiles based on radial flow experiments: A benchmark exercise, Composites Part A: Applied Science and Manufacturing 121 (March) (2019) 100–114. doi:10.1016/j.compositesa.2019.03.006. 16

[102] A. X. Yong, A. Aktas, D. May, A. Endruweit, S. Advani, P. Hubert, S. G. Abaimov, D. Abliz, I. Akhatov, M. A. Ali, T. Allen, D. C. Berg, S. Bickerton, C. Brauner, D. Brütsch, B. Caglar, H. Caglar, P. Causse, A. Chiminelli, A. Cohades, S. Comas-Cardona, M. Danzi, J. Dittmann, C. Dransfeld, P. Ermanni, E. Fauster, J. A. Garcia-Manrique, A. George, R. Graupner, V. Grishaev, A. Guilloux, M. Hancioglu, W. Harizi, T. Herman, W. Huang, M. A. Kabachi, A. Keller, K. Kind, M. Laspalas, O. V. Lebedev, M. Lizaranzu, A. C. Long, K. Masania,

V. Michaud, P. Middendorf, D. Salvatori, R. Schubnel, N. Sharp, M. Sozer, J. Thomas, F. Trochu, R. Umer, J. Valette, J. H. Wang, B. Willenbacher, Out-of-plane permeability measurement for reinforcement textiles: A benchmark exercise, Composites Part A: Applied Science and Manufacturing 148 (2021) 106480. doi:10.1016/J.COMPOSITESA.2021.106480. 16

[103] S. L. Simon, G. B. Mckenna, O. Sindt, Modeling the evolution of the dynamic mechanical properties of a commercial epoxy during cure after gelation, Journal of Applied Polymer Science 76 (4) (2000) 495–508. doi:10.1002/(SICI)1097-4628(20000425)76:4<495::AID-APP7>3.0.CO;2-B. 18

[104] K. S. Kim, H. T. Hahn, Residual stress development during processing of graphite/epoxy composites, Composites Science and Technology 36 (2) (1989) 121–132. doi:10.1016/0266-3538(89)90083-3. 18

[105] D. Radford, R. Diefendorf, Shape Instabilities in Composites Resulting from Laminate Anisotropy, Journal of Reinforced Plastics and Composites 12 (1) (1993) 58–75. doi:10.1177/073168449301200104.

[106] D. W. Radford, T. S. Rennick, Separating sources of manufacturing distortion in laminated composites, Journal of Reinforced Plastics and Composites 19 (8) (2000) 621–641. doi:10.1106/CRMP-ARE5-GVPP-0Y7N.

[107] M. Wisnom, M. Gigliotti, N. Ersoy, M. Campbell, K. Potter, Mechanisms generating residual stresses and distortion during manufacture of polymer–matrix composite structures, Composites Part A: Applied Science and Manufacturing 37 (4) (2006) 522–529. doi:10.1016/j.compositesa.2005.05.019.

[108] S. White, H. Hahn, Cure Cycle Optimization for the Reduction of Processing-Induced Residual Stresses in Composite Materials, Journal of Composite Materials 27 (14) (1993) 1352–1378. doi:10.1177/002199839302701402.

[109] N. Ersoy, M. Tugutlu, Cure kinetics modeling and cure shrinkage behavior of a thermosetting composite, Polymer Engineering & Science 50 (1) (2010) 84–92. doi:10.1002/pen.21514. 18

[110] J. R. Wood, M. G. Bader, Void control for polymer-matrix composites (1): Theoretical and experimental methods for determining the growth and collapse of gas bubbles, Composites Manufacturing 5 (3) (1994) 139–147. doi:10.1016/0956-7143(94)90023-X. 18

[111] T. Lundström, Measurement of void collapse during resin transfer moulding, Composites Part A: Applied Science and Manufacturing 28 (3) (1997) 201–214. doi:10.1016/S1359-835X(96)00109-1.

[112] C. Pupin, A. Ross, C. Dubois, J.-C. Rietsch, N. Vernet, E. Ruiz, Formation and suppression of volatile-induced porosities in an RTM epoxy resin, Composites Part A: Applied Science and Manufacturing 94 (2017) 146–157. doi:10.1016/j.compositesa.2016.12.006. 18, 20

[113] C. Pupin, Développement d'outils de prévision de la porosité résiduelle d'origine chimique destinés à l'optimisation des paramètres de fabrication de pièces composites structurales en RTM, Ph.D. thesis, École polytechnique de montréal (2017). 18

[114] A. C. Loos, G. S. Springer, Curing of Epoxy Matrix Composites, Journal of Composite Materials 17 (2) (1983) 135–169. doi:10.1177/002199838301700204. 18

[115] J. M. Svanberg, J. A. Holmberg, Prediction of shape distortions Part I. FE-implementation of a path dependent constitutive model, Composites Part A: Applied Science and Manufacturing 35 (6) (2004) 711–721. doi:10.1016/j.compositesa.2004.02.005. 18, 22

[116] T. A. Bogetti, J. W. Gillespie, Process-Induced Stress and Deformation in Thick-Section Thermoset Composite Laminates, Journal of Composite Materials 26 (5) (1992) 626–660. doi:10.1177/002199839202600502. 18

[117] M. Benavente, L. Marcin, A. Courtois, M. Lévesque, E. Ruiz, Viscoelastic distortion in asymmetric plates during post curing, Composites Part A: Applied Science and Manufacturing 103 (2017) 122–130. doi:10.1016/j.compositesa.2017.09.017. 18, 19, 21, 27

[118] D. Adolf, R. Chambers, Verification of the capability for quantitative stress prediction during epoxy cure, Polymer 38 (21) (1997) 5481–5490. doi:10.1016/S0032-3861(97)00077-3. 18

[119] Y. Abou Msallem, F. Jacquemin, N. Boyard, A. Poitou, D. Delaunay, S. Chatel, Material characterization and residual stresses simulation during the manufacturing process of epoxy

matrix composites, Composites Part A: Applied Science and Manufacturing 41 (1) (2010) 108–115. doi:10.1016/j.compositesa.2009.09.025.

[120] L. L. Khoun, R. De Oliveira, V. V. Michaud, P. Hubert, Investigation of process-induced strains development by fibre Bragg grating sensors in resin transfer moulded composites, Composites Part A: Applied Science and Manufacturing 42 (3) (2011) 274–282. doi:10.1016/j.compositesa.2010.11.013. 18

[121] N. Zobeiry, A. Forghani, C. Li, K. Gordnian, R. Thorpe, R. Vaziri, G. Fernlund, A. Poursartip, Multiscale characterization and representation of composite materials during processing, Philosophical Transactions of the Royal Society A: Mathematical, Physical and Engineering Sciences 374 (2071) (2016). doi:10.1098/rsta.2015.0278. 18, 19

[122] A. A. Johnston, An Integrated Model of the Development of Process-Induced Deformation in Autoclave Processing of Composite Structures, Ph.D. thesis, THE UNIVERSITY OF BRITISH COLUMBIA (1998). doi:10.14288/1.0088805. 18, 27

[123] Q. Wang, T. Li, X. Yang, Q. Huang, B. Wang, M. Ren, Multiscale numerical and experimental investigation into the evolution of process-induced residual strain/stress in 3D woven composite, Composites Part A: Applied Science and Manufacturing 135 (aug 2020). doi:10.1016/j.compositesa.2020.105913. 19, 27

[124] A. Ding, S. Li, J. Sun, J. Wang, L. Zu, A thermo-viscoelastic model of process-induced residual stresses in composite structures with considering thermal dependence, Composite Structures 136 (2016) 34–43. 19

[125] M. A. Biot, Theory of stress-strain relations in anisotropic viscoelasticity and relaxation phenomena, Journal of Applied Physics 25 (11) (1954) 1385–1391. doi:10.1063/1.1721573. 19

[126] R. A. Schapery, Application of thermodynamics to thermomechanical, fracture, and birefringent phenomena in viscoelastic media, Journal of Applied Physics 35 (5) (1964) 1451–1465. doi:10.1063/1.1713649.

[127] M. Lévesque, K. Derrien, D. Baptiste, M. D. Gilchrist, On the development and parameter

identification of Schapery-type constitutive theories, Mechanics of Time-Dependent Materials 12 (2) (2008) 95–127. doi:10.1007/s11043-008-9052-y. 19

[128] Q. Zhu, P. Shrotriya, N. R. Sottos, P. H. Geubelle, Three-dimensional viscoelastic simulation of woven composite substrates for multilayer circuit boards, Composites Science and Technology 63 (13) (2003) 1971–1983. doi:10.1016/S0266-3538(03)00171-4. 19

[129] Y. Cai, H. Sun, Thermo-viscoelastic analysis of three-dimensionally braided composites, Composite Structures 98 (2013) 47–52. doi:10.1016/j.compstruct.2012.11.012.

[130] J. jun Zhai, X. xia Kong, S. Cheng, X. hong Wang, H. ming Cheng, A coupled multi-scale method for predicting the viscoelastic behavior of resin-based 3D braided composites, Materials and Design 195 (2020) 109048. doi:10.1016/j.matdes.2020.109048.

[131] L. Ge, H. Li, Y. Zhang, J. Zhong, Y. Chen, D. Fang, Multiscale viscoelastic behavior of 3D braided composites with pore defects, Composites Science and Technology 217 (June 2021) (2022) 109114. doi:10.1016/j.compscitech.2021.109114.

[132] Y. Fu, X. Gao, X. Yao, Mesoscopic simulation on curing deformation and residual stresses of 3D braided composites, Composite Structures 246 (February) (2020) 112387. doi:10.1016/j.compstruct.2020.112387. 19

[133] A. Courtois, M. Hirsekorn, M. Benavente, A. Jaillon, L. Marcin, E. Ruiz, M. Lévesque, Viscoelastic behavior of an epoxy resin during cure below the glass transition temperature: Characterization and modeling, Journal of Composite Materials 53 (2) (2018) 155–171. doi:10.1177/0021998318781226. 19

[134] A. Courtois, L. Marcin, M. Benavente, E. Ruiz, M. Lévesque, Numerical multiscale homogenization approach for linearly viscoelastic 3D interlock woven composites, International Journal of Solids and Structures 163 (2019) 61–74. doi:10.1016/j.ijsolstr.2018.12.018. 19, 20, 27

[135] A. Trofimov, C. Tuloup, J. Le Pavic, C. Ravey, D. Therriault, M. Lévesque, Multi-scale modeling of process-induced pressure distribution inside 3D woven composites manufactured using Resin Transfer Molding, Composites Part A: Applied Science and Manufacturing (2022) 107307doi:10.1016/j.compositesa.2022.107307. 20, 21, 27

[136] K. Vasylevskyi, I. Tsukrov, B. Drach, H. Buntrock, T. Gross, Identification of process-induced residual stresses in 3D woven carbon/epoxy composites by combination of FEA and blind hole drilling, Composites Part A: Applied Science and Manufacturing 130 (December 2019) (2020) 105734. doi:10.1016/j.compositesa.2019.105734. 21, 27

[137] J. M. Lawrence, M. Devillard, S. G. Advani, An approach to couple mold design and on-line control to manufacture complex composite parts by resin transfer molding, Annual Technical Conference - ANTEC, Conference Proceedings 2 (2003) 2079–2083. 24

[138] O. Restrepo, K.-T. Hsiao, A. Rodriguez, B. Minaie, Development of adaptive injection flow rate and pressure control algorithms for resin transfer molding, Composites Part A: Applied Science and Manufacturing 38 (6) (2007) 1547–1568. doi:10.1016/j.compositesa.2007.01.005.

[139] E. Sozer, S. Bickerton, S. Advani, On-line strategic control of liquid composite mould filling process, Composites Part A: Applied Science and Manufacturing 31 (12) (2000) 1383–1394. doi:10.1016/S1359-835X(00)00060-9.

[140] S. Bickerton, H. C. Stadtfeld, K. V. Steiner, S. G. Advani, Design and application of actively controlled injection schemes for resin-transfer molding, Composites Science and Technology 61 (11) (2001) 1625–1637. doi:10.1016/S0266-3538(01)00064-1.

[141] M. Torres, Parameters' monitoring and in-situ instrumentation for resin transfer moulding: A review, Composites Part A: Applied Science and Manufacturing 124 (2019) 105500. doi:10.1016/j.compositesa.2019.105500. 24

[142] R. F. Benenati, Process modeling, simulation and control for chemical engineers, William L. Luyben, McGraw-Hill, New York, 1973. 558 pp., Journal of Polymer Science: Polymer Letters Edition 11 (4) (1973) 289–290. doi:10.1002/pol.1973.130110416. 24

[143] K. Deb, Optimization for Engineering Design: Algorithms and Examples, 2nd Edition, New Delhi, New Delhi, 2012. 24

[144] G. Struzziero, J. J. Teuwen, A. A. Skordos, Numerical optimisation of thermoset composites manufacturing processes: A review, Composites Part A: Applied Science and Manufacturing 124 (March) (2019) 105499. doi:10.1016/j.compositesa.2019.105499. 24, 25, 28

[145] B. X. Chai, B. Eisenbart, M. Nikzad, B. Fox, A. Blythe, P. Blanchard, J. Dahl, Simulation-based optimisation for injection configuration design of liquid composite moulding processes: A review, Composites Part A: Applied Science and Manufacturing 149 (June) (2021) 106540. doi:10.1016/j.compositesa.2021.106540. 25

[146] A. Zade, R. R. P. Kuppusamy, A review on numerical optimization in liquid composite moulding processes, Materials Today: Proceedings 19 (2019) 329–332. doi:10.1016/j.matpr.2019.07.605. 24

[147] R. L. Keeney, H. Raiffa, R. F. Meyer, Decisions with multiple objectives: preferences and value trade-offs, Cambridge University Press, 1993. 24

[148] J. H. Holland, Adaptation in natural and artificial systems: an introductory analysis with applications to biology, control, and artificial intelligence, MIT press, 1992. 25

[149] J. Kennedy, Particle swarm: Social adaptation of knowledge, in: Proceedings of the IEEE Conference on Evolutionary Computation, ICEC, 1997, pp. 303–308. doi:10.1109/icec.1997.592326. 25

[150] M. Dorigo, L. M. Gambardella, Ant colony system: A cooperative learning approach to the traveling salesman problem, IEEE Transactions on Evolutionary Computation 1 (1) (1997) 53–66. doi:10.1109/4235.585892. 25

[151] S. Jiang, C. Zhang, B. Wang, Optimum arrangement of gate and vent locations for RTM process design using a mesh distance-based approach, Composites Part A: Applied Science and Manufacturing 33 (4) (2002) 471–481. doi:10.1016/S1359-835X(01)00146-4. 25, 28

[152] A. Gokce, S. Advani, Combinatorial search to optimize vent locations in the presence of disturbances in liquid composite molding processes, Materials and Manufacturing Processes 18 (2) (2003) 261–285. doi:10.1081/AMP-120018909.

[153] A. Gokce, S. G. Advani, Vent Location Optimization Using Map-Based Exhaustive Search in Liquid Composite Molding Processes, Materials and Manufacturing Processes 19 (3) (2004) 523–548. doi:10.1081/AMP-120038659. 25

[154] R. Mathur, S. G. Advani, B. K. Fink, Use of genetic algorithms to optimize gate and vent locations for the resin transfer molding process, Polymer Composites 20 (2) (1999) 167–178. doi:10.1002/pc.10344.

[155] G. Struzziero, A. A. Skordos, Multi-objective optimization of Resin Infusion, Advanced Manufacturing: Polymer and Composites Science 5 (1) (2019) 17–28. doi:10.1080/20550340.2019.1565648. 25

[156] B. Y. Kim, G. J. Nam, J. W. Lee, Optimization of filling process in RTM using genetic algorithm, Korea Australia Rheology Journal 12 (1) (2000) 83–92. 25

[157] J. Spoerre, C. Zhang, B. Wang, R. Parnas, Integrated Product and Process Design for Resin Transfer Molded Parts, Journal of Composite Materials 32 (13) (1998) 1244–1272. doi:10.1177/002199839803201301.

[158] J. Gou, C. Zhang, Z. Liang, B. Wang, J. Simpson, Resin transfer molding process optimization using numerical simulation and design of experiments approach, Polymer Composites 24 (1) (2003) 1–12. doi:10.1002/pc.10000. 25, 28

[159] E. Ruiz, F. Trochu, Multi-criteria thermal optimization in liquid composite molding to reduce processing stresses and cycle time, Composites Part A: Applied Science and Manufacturing 37 (6 SPEC. ISS.) (2006) 913–924. doi:10.1016/j.compositesa.2005.06.010. 25, 26, 28

[160] K. I. Tifkitsis, T. S. Mesogitis, G. Struzziero, A. A. Skordos, Stochastic multi-objective optimisation of the cure process of thick laminates, Composites Part A: Applied Science and Manufacturing 112 (April) (2018) 383–394. doi:10.1016/j.compositesa.2018.06.015. 26

[161] H.-W. Yu, W.-B. Young, Optimal Design of Process Parameters for Resin Transfer Molding, Journal of Composite Materials 31 (11) (1997) 1113–1140. doi:10.1177/002199839703101103. 25

[162] N. G. Pantelelis, Optimised cure cycles for resin transfer moulding, Composites Science and Technology 63 (2) (2003) 249–264. doi:10.1016/S0266-3538(02)00196-3.

[163] G. Struzziero, A. A. Skordos, Multi-objective optimisation of the cure of thick components, Composites Part A: Applied Science and Manufacturing 93 (2017) 126–136. doi:10.1016/j.compositesa.2016.11.014. 25, 26

[164] X. Hui, Y. Xu, W. Zhang, W. Zhang, Multiscale collaborative optimization for the thermochemical and thermomechanical cure process during composite manufacture, Composites Science and Technology 224 (January) (2022) 109455. doi:10.1016/j.compscitech.2022.109455. 26, 27, 28

[165] D. Dolkun, W. Zhu, Q. Xu, Y. Ke, Optimization of cure profile for thick composite parts based on finite element analysis and genetic algorithm, Journal of Composite Materials 52 (28) (2018) 3885–3894. doi:10.1177/0021998318771458. 25, 26, 28

[166] Q. Wang, X. Yang, H. Zhao, X. Zhang, G. Cao, M. Ren, Microscopic residual stresses analysis and multi-objective optimization for 3D woven composites, Composites Part A: Applied Science and Manufacturing 144 (January) (2021) 106310. doi:10.1016/j.compositesa.2021.106310. 25, 26, 27, 28

[167] S. Cassola, M. Duhovic, T. Schmidt, D. May, Machine learning for polymer composites process simulation – a review, Composites Part B: Engineering 246 (2022) 110208. doi:10.1016/J.COMPOSITESB.2022.110208. 27

[168] B. Caglar, G. Broggi, M. A. Ali, L. Orgéas, V. Michaud, Deep learning accelerated prediction of the permeability of fibrous microstructures, Composites Part A: Applied Science and Manufacturing 158 (2022) 106973. doi:10.1016/J.COMPOSITESA.2022.106973. 27

[169] L. Gélébart, J. Dérouillat, Simulations FFT massivement parallèles en mécanique des matériaux hétérogènes, in: 13e colloque national en calcul des structures, 2017. 29

[170] H. Moulinec, P. Suquet, A numerical method for computing the overall response of nonlinear composites with complex microstructure, Computer Methods in Applied Mechanics and Engineering 157 (1-2) (1998) 69–94. doi:10.1016/S0045-7825(97)00218-1. 29